AGU PUBLICATIONS

JGR

Journal of Geophysical Research: Planets

RESEARCH ARTICLE
10.1002/2016JE005133

Special Section:
Investigations of the Bagnold Dune Field, Gale crater

Key Points:
- Spectral variability in the dunes arises from spatially variable mineral composition and qualitatively correlates with local sand flux
- Mineral abundance estimates from orbit are within <13 wt % of in situ measurements from CheMin in average, although uncertainties are large
- Orbital observations of dune field mineral variations may be explained by both aeolian sorting and mixing of multiple sand sources

Correspondence to:
M. G. A. Lapotre,
mlapotre@caltech.edu

Citation:
Lapotre, M. G. A., B. L. Ehlmann, S. E. Minson, R. E. Arvidson, F. Ayoub, A. A. Fraeman, R. C. Ewing, and N. T. Bridges (2017), Compositional variations in sands of the Bagnold Dunes, Gale crater, Mars, from visible-shortwave infrared spectroscopy and comparison with ground truth from the Curiosity rover, *J. Geophys. Res. Planets*, *122*, 2489–2509, doi:10.1002/2016JE005133.

Received 13 JUL 2016
Accepted 26 JAN 2017
Accepted article online 14 APR 2017
Published online 7 DEC 2017

Compositional variations in sands of the Bagnold Dunes, Gale crater, Mars, from visible-shortwave infrared spectroscopy and comparison with ground truth from the Curiosity rover

M. G. A. Lapotre[1], B. L. Ehlmann[1,2], S. E. Minson[3], R. E. Arvidson[4], F. Ayoub[1], A. A. Fraeman[2], R. C. Ewing[5], and N. T. Bridges[6]

[1]Division of Geological and Planetary Sciences, California Institute of Technology, Pasadena, California, USA, [2]Jet Propulsion Laboratory, California Institute of Technology, Pasadena, California, USA, [3]U.S. Geological Survey Earthquake Science Center, Menlo Park, California, USA, [4]Department of Earth and Planetary Sciences, Washington University, St. Louis, Missouri, USA, [5]Department of Geology and Geophysics, Texas A&M University, College Station, Texas, USA, [6]Applied Physics Laboratory, The Johns Hopkins University, Laurel, Maryland, USA

Abstract During its ascent up Mount Sharp, the Mars Science Laboratory Curiosity rover traversed the Bagnold Dune Field. We model sand modal mineralogy and grain size at four locations near the rover traverse, using orbital shortwave infrared single-scattering albedo spectra and a Markov chain Monte Carlo implementation of Hapke's radiative transfer theory to fully constrain uncertainties and permitted solutions. These predictions, evaluated against in situ measurements at one site from the Curiosity rover, show that X-ray diffraction-measured mineralogy of the basaltic sands is within the 95% confidence interval of model predictions. However, predictions are relatively insensitive to grain size and are nonunique, especially when modeling the composition of minerals with solid solutions. We find an overall basaltic mineralogy and show subtle spatial variations in composition in and around the Bagnold Dunes, consistent with a mafic enrichment of sands with cumulative aeolian-transport distance by sorting of olivine, pyroxene, and plagioclase grains. Furthermore, the large variations in Fe and Mg abundances (~20 wt %) at the Bagnold Dunes suggest that compositional variability may be enhanced by local mixing of well-sorted sand with proximal sand sources. Our estimates demonstrate a method for orbital quantification of composition with rigorous uncertainty determination and provide key constraints for interpreting in situ measurements of compositional variability within Martian aeolian sandstones.

1. Introduction

Gale crater was chosen as the landing site for the Mars Science Laboratory (MSL) Curiosity rover because of its well-defined sedimentary rock record, inferred to span a major climate change and drying of the Martian surface environment [e.g., *Anderson and Bell III*, 2010; *Milliken et al.*, 2010]. Gale crater also contains dark mafic sands accumulating on the crater floor as sand sheets and sand dunes (Figure 1a) with some fraction of the grains blown out of the crater to the south [*Anderson and Bell III*, 2010; *Day and Kocurek*, 2016; *Day et al.*, 2016]. The Curiosity rover drove through a topographic low within the broad expanse of bedrock that defines the base of Mount Sharp (officially named Aeolis Mons), which is the principal target of Curiosity's investigation. Mafic sands accumulated near this topographic low form a dune field, informally named the Bagnold Dune Field (Figure 1a). The Bagnold Dunes are morphologically diverse: individual barchan dunes at the upwind (or trailing) margin migrate to the southwest, merge into barchanoidal ridges downwind, and ultimately transition into linear dunes paralleling the foothills of Mount Sharp (Figure 1a). Average wind directions inferred from the orientation of dunes [e.g., *Hobbs et al.*, 2010; *Silvestro et al.*, 2013; *Day and Kocurek*, 2016] and ventifacts [*Bridges et al.*, 2014] are mostly from northeast to southwest near the rover path.

Sand composition in Gale crater was modeled to be olivine-rich [e.g., *Rogers and Bandfield*, 2009] and later estimated to contain olivine of forsterite number (Fo) ~55 [*Lane and Christensen*, 2013], using data from the Thermal Emission Spectrometer, acquired at a resolution of approximately 3 × 6 km/pixel. Spectral variability in the visible-to-shortwave infrared (VSWIR) wavelength range was observed at a finer spatial resolution (18 m/pixel) from Compact Reconnaissance Imaging Spectrometer for Mars (CRISM) data acquired in the northeast portion of the dune field, near Curiosity's landing site [*Seelos et al.*, 2014]. The barchan dunes

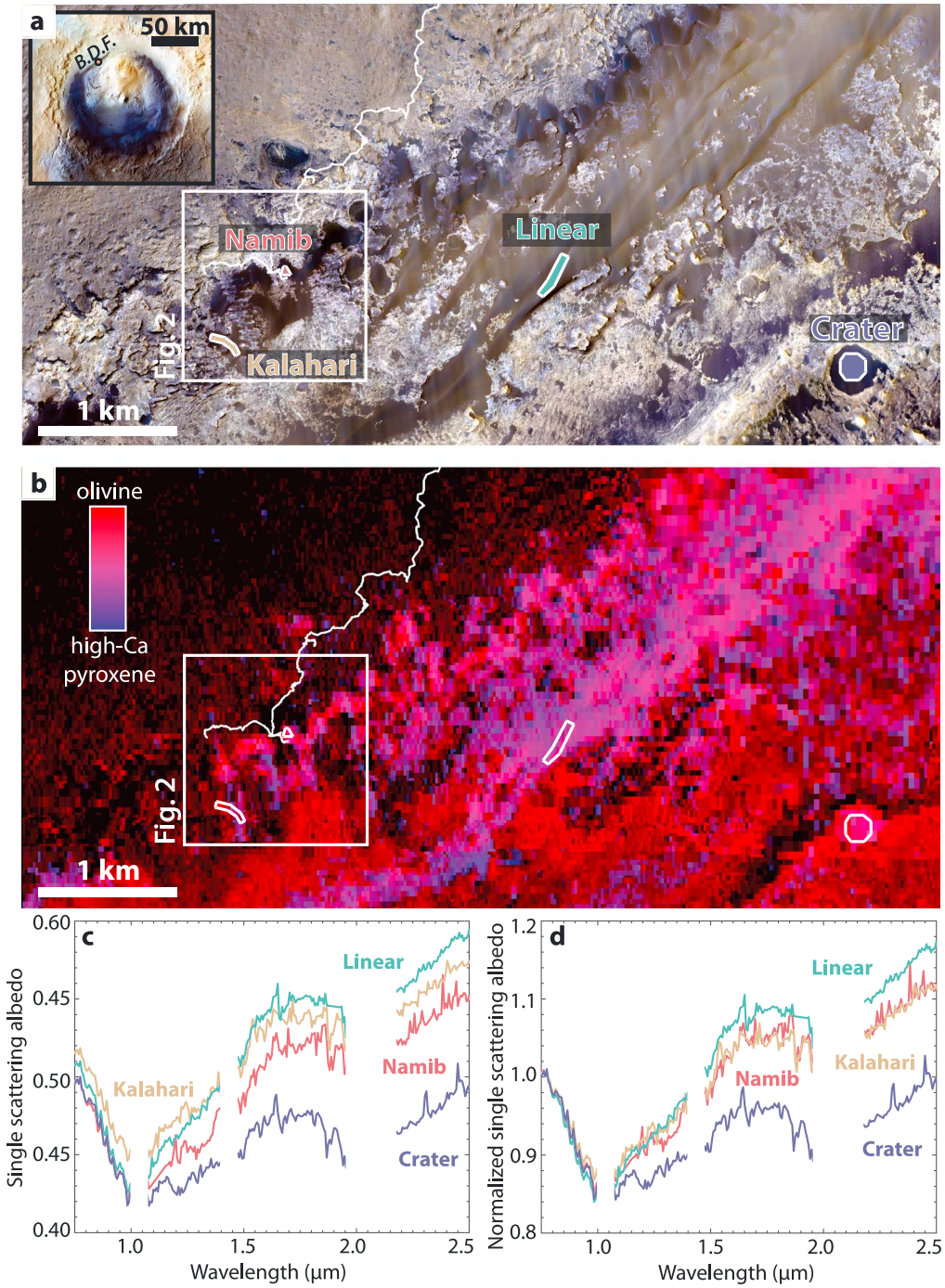

Figure 1. (a) HiRISE context map of the Bagnold Dunes of Gale crater, Mars, with Regions of Interest (ROIs) and the traverse of the Curiosity rover up to sol 1371 (thin white line). The inset shows the location of the study area (orange circle) on a Context Camera/High Resolution Stereo Camera/Viking composite image of Gale crater, Mars (centered on −4.983°N, 137.765°E; credit: NASA/Jet Propulsion Laboratory-California Institute of Technology/European Space Agency/Deutsches Zentrum für Luft- und Raumfahrt/Freie Universität Berlin/ Malin Space Science Systems); the Bagnold Dune Field is labeled B.D.F. The white box outlines the extent of Figures 2a–2c. (b) Composite CRISM parameter map near the rover traverse within the Bagnold Dune Field with ROIs and the traverse of the Curiosity rover up to sol 1371 (thin white line). The red hues indicate relatively high values of OLINDEX3, i.e., stronger olivine signatures, while the blue hues correspond to relatively high values of HCPINDEX2, i.e., stronger high-Ca pyroxene signatures [e.g., *Viviano-Beck et al.*, 2014]. ROIs are outlined. The white box outlines the extent of Figures 2a–2c. (c) Raw and (d) normalized single-scattering albedo spectra of the ROIs herein investigated—Namib Dune, Kalahari Dune, a linear dune, and a crater fill. Spectra in Figure 1d were normalized by their SSA at 0.8 μm to highlight differences in continuum spectral slopes at longer wavelengths.

and the crests of linear dunes have stronger olivine signatures, while the stoss sides of barchanoidal ridges have stronger high-Ca pyroxene signatures (Figures 1b–1d). These observations likely indicate spatial variability in composition and may result from several mechanisms, including variable dust cover, mixing of different sediment sources, and/or wind sorting of mineral phases by grain size, density, and shape.

Wind sorting has been suggested at various places around Mars. For example, *Chojnacki et al.* [2013] demonstrated variability in the iron oxidation state of materials in sand dunes due to local aeolian fractionation at Capri Chasma and Melas Chasma from High Resolution Imaging Science Experiment (HiRISE) band ratios. Variability in thermal inertia was observed by *Pan and Rogers* [2017] within several dune fields on Mars, indicating spatially inhomogeneous grain-size distributions. Global comparisons of sand composition have been made and showed that dark Martian sands are primarily mafic with some compositional variation [*Poulet et al.*, 2009; *Tirsch et al.*, 2011]. However, quantitative estimates of variability in modal mineral composition and grain sizes in Martian dune fields largely remain to be performed.

The composition of aeolian sedimentary rocks not only reflects that of the sediment source(s) but also subsequent modifications of the primary composition by sorting during transport and postburrial diagenesis and alteration. Thus, a quantitative understanding of the degree of sand-sorting by Martian winds is critical to the interpretation of in situ measurements of the compositional variability of aeolian sedimentary rocks, which have been observed both from orbit [*Milliken et al.*, 2014] and in situ with rovers [*Grotzinger et al.*, 2005; *Siebach et al.*, 2017].

In this paper, we analyze orbiter-based data to qualitatively map the spectral variability within the Bagnold Dune Field near the rover traverse (Figures 1b–1d) as well as invert for quantitative sand bulk composition and grain sizes at four unique locations—the Namib and Kalahari Dunes, a linear dune, and a crater fill (Figure 1a). We compare our orbital inferences with ground observations from the Curiosity rover at Namib Dune (Figure 1a) and infer the magnitude and causes of compositional variations observed from orbit.

2. Methods

2.1. Derived Orbital Data Products

CRISM measures radiance reflected from the Martian surface at 544 discrete wavelengths from ~0.4 to 4.0 μm [*Murchie et al.*, 2009]. Full-resolution targeted (FRT) CRISM scenes have spatial resolutions of ~18 m/pixel, and along-track oversampled (ATO) scenes can be acquired and processed with spatial resolutions of ~12 m/pixel or less [e.g., *Arvidson et al.*, 2015; *Kreisch et al.*, 2017]. Surface single-scattering albedo (SSA) spectra were retrieved from measured I/F (CRISM image ATO0002EC79) by use of a look-up table. The latter was derived by using a discrete ordinates radiative transfer model (DISORT) of atmospheric contributions from CO_2, CO, H_2O, dust, and ice aerosols [*Stamnes et al.*, 1988], and a Martian surface scattering function [*Johnson et al.*, 2006a, 2006b; *Sullivan et al.*, 2008; *Arvidson et al.*, 2014; *Kreisch et al.*, 2017].

We consider a set of dunes and sand fills near Curiosity's traverse (Figure 1a). VSWIR spectra of four regions of interest (ROIs)—two barchan dunes (Namib and Kalahari), a linear dune, and a crater fill (Figure 1a)—were selected to be inverted for modal mineralogy. These four sites were chosen because they are most distinct in terms of their overall spectral properties (i) near the rover traverse (Namib and Kalahari) and (ii) within the entire spectral scene (linear dune and crater). We averaged atmospherically corrected single-scattering albedo spectra over four ROIs, composed of 74, 127, 222, and 284 CRISM ATO pixels on Namib Dune, Kalahari Dune, the linear dune, and the crater fill, respectively (Figure 1a). Figures 1c and 1d show the raw and normalized spectra at the four locations. Masked wavelength regions were removed from our analysis because they contained spurious atmospheric residuals.

Variations in spectral properties can also be tracked over a broad area. Spatial variability in olivine and pyroxene abundance was examined with 18 m/pixel FRT CRISM data and a series of spectral parameters, including the olivine index 3 (OLINDEX3) (Figure 2a), which increases with the strength of the 1 μm olivine spectral absorption and is used as a proxy for olivine content and/or grain size [*Viviano-Beck et al.*, 2014]. The ferrous versus ferric nature of surface materials was mapped at 0.3 m/pixel, using a red/infrared band ratio from HiRISE scenes ESP_021610_1755 and ESP_035772_1755 (Figure 2b) [*Delamere et al.*, 2010]. HiRISE red/infrared band ratios are low for ferric (typically dust-covered) and high for ferrous materials (mafic surfaces). Ripple displacements were estimated near the traverse of the Curiosity rover from a time

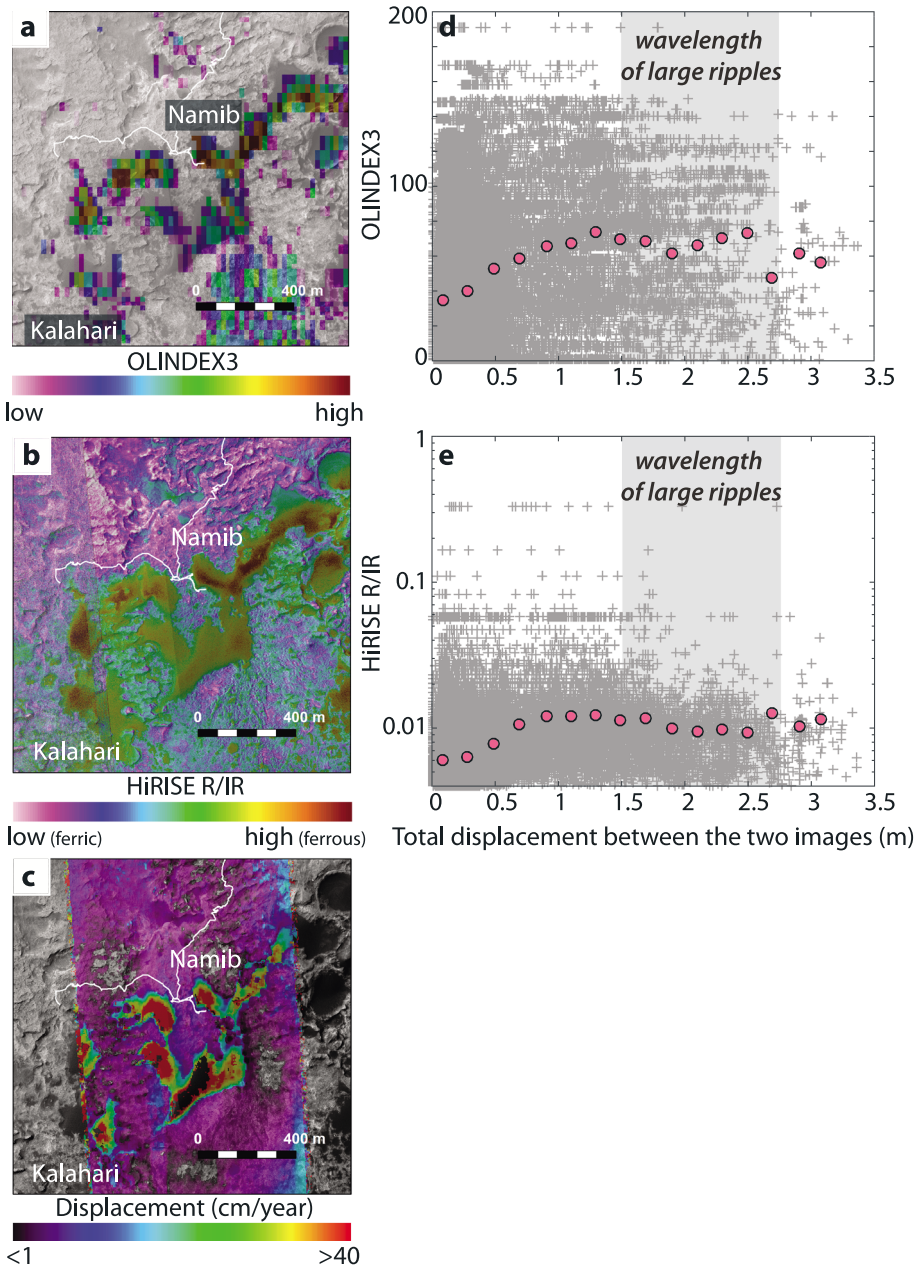

Figure 2. Maps of (a) OLINDEX3, (b) HiRISE red/infrared band ratio, and (c) ripple displacements derived from HiRISE image pairs. The white sinuous line shows the traverse of the Curiosity rover up to sol 1371. (d) Scatterplot of OLINDEX3 versus total ripple displacements and (e) scatterplot of HiRISE red/infrared band ratio versus total ripple displacements. The pink circles represent binned data (means). The shaded zones outline the range of large ripple wavelengths at the Bagnold Dunes [*Lapotre et al.*, 2016].

correlation of a HiRISE stereo-pair (ESP_018854_1755, acquired 04 August 2010, and ESP_035772_1755, acquired 14 March 2014), following the technique of *Bridges et al.* [2012], over a total timespan of 1318 Earth days (Figure 2c). This technique relies on the movement of ripples exclusively as a proxy for sand flux [e.g., *Ayoub et al.*, 2014].

2.2. Quantitative Mineralogy Using a Bayesian Implementation of the Hapke Radiative Transfer Model

Radiative transfer models [e.g., *Hapke*, 1981] allow inversion of single-scattering albedo spectra of planetary surfaces for mineral abundance and grain sizes. Though prior authors have typically presented only a single

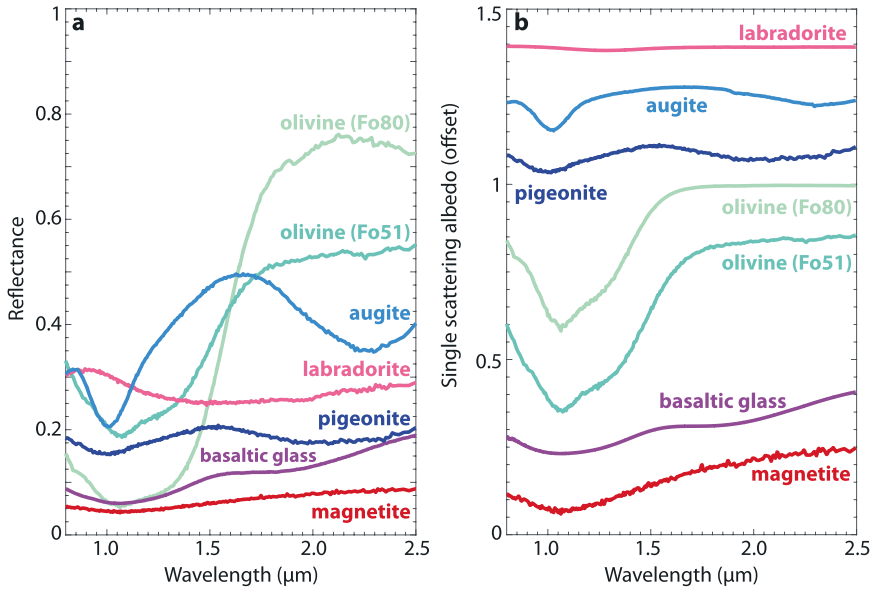

Figure 3. (a) Laboratory reflectance spectra of the mineral endmembers used in our inversion of modal mineralogy, and (b) corresponding single-scattering albedos calculated for a grain size of 100 μm, and vertically offset for clarity. Sources of the spectra are summarized in Table 1.

best fit solution to estimate mineral abundances, the solution to the inverse problem is highly nonunique due to parameter trade-offs, e.g., between the abundances of different mineral endmembers and between abundance and grain size of a same mineral endmember. Moreover, noise in the data adds to the uncertainty in selecting a best fit solution [e.g., *Lapotre et al.*, 2017]. In order to allow for a range of modal mineralogies that could reasonably explain the data, given its noise, and to estimate the uncertainty associated with the nonuniqueness of the inversion technique, we adapted a Markov chain Monte Carlo (MCMC) algorithm originally implemented to invert for seismic slip along faults [*Minson et al.*, 2013; *Minson et al.*, 2014] to the radiative transfer inverse problem [*Lapotre et al.*, 2017]. Specifically, the forward model used to estimate the likelihood of a given sample given the data is the geometric optic model for light scattering of *Hapke* [1981]. The MCMC technique allows us to explore the parameter space (mineral abundances and grain sizes) at a sampling density that is proportional to the likelihood of a model given the data, which is a function of the misfit between the modeled spectrum and the data. Consequently, histograms of all accepted model solutions yield the probability densities associated with abundance and grain size of each mineral constituent.

Our general approach in selecting mineral endmembers was to assume no a priori knowledge on their precise chemical compositions and to determine a parsimonious set of endmembers. Thus, our suite of mineral endmembers was selected on the basis of (i) some of them being optically active and obviously required (e.g., olivine and pyroxenes) and (ii) others being expected in the context of mafic Martian sands and/or consistent with initial tests suggesting their necessity to fit the data properly (e.g., plagioclase, magnetite, hematite, and basaltic glass). In preliminary inversions, we tested the quality of fits to the data using six olivines of variable composition (Fo numbers ranging from 51 to 91), four pyroxenes of variable Ca content (enstatite to diopside), two plagioclases (andesine and labradorite), magnetite, hematite, and a basaltic glass. Hematite did not significantly improve the spectral fits and was thus removed for the sake of parsimony. Similarly, solid solutions that yielded poor fit residuals were discarded. Our final set of mineral endmembers to model the composition of sands of the Bagnold Dunes include one olivine, two pyroxenes (augite and pigeonite), a plagioclase (labradorite), magnetite, and basaltic glass (Figure 3 and Table 1). Orthopyroxenes and higher Ca pyroxenes produced poorer fits to the 2 μm feature. The higher reflectance plagioclase produced better fits. Multiple olivines were possible, but the Fo51 olivine produced slightly better fits. We show results for both Fo51 olivine (preferred) and Fo80 to illustrate the sometimes subtle effects of mineral solid solution.

The propagation of light in absorbing materials is typically described by a complex-valued index of refraction, with a real part (n), which accounts for reflection and refraction, and an imaginary part (k), which accounts for

Table 1. Mineral Endmembers, Assumed Densities, Allowed Grain-Size Ranges, and Assumed Real Index of Refraction[a]

Mineral Endmember		Density (kg/m^3)	Grain-Size Range Allowed (μm)	Real Index of Refraction (n)	Source	Grain-Size Range of Library Sample (μm)	Grain Size Used to Calculate k (μm)
Olivine	Fo51	3320	50–800	1.67	KI3188[c]	<60	25
	Fo80	3320	50–800	1.67	HS285.4B[c]	250–1200	300
Augite		3400	50–800	1.70	NMNH120049[c]	<60	35
Pigeonite		3380	50–800	1.70	HS199.3B[c]	75–250	162
Labradorite[b]		2690	50–800	1.56	HS17.3B[c]	75–250	162
Magnetite		5150	10–200	2.42	HS195.3B[c]	75–250	162
Basaltic glass		2780	50–800	1.50	C1BE100[d]	45–75	60

[a]The endmember spectra we selected from the U.S. Geological Survey Spectral Library [*Clark et al.*, 2007] were acquired with a Beckman spectrometer in directional conical mode, with a measured average phase angle of 30°; we thus assumed an incidence angle of 30° and emission angle of 0° for those spectra.
[b]Contains magnetite as disseminated microscopic impurities.
[c]*Clark et al.* [2007].
[d]RELAB Brown/Nasa-Keck spectral library.

absorption. Together, n and k are wavelength-dependent properties of a given material and are colloquially referred to as optical constants. Within the wavelength range we consider (0.8–2.5 μm), we assume that the real index of refraction, n, of our mineral endmembers is a constant [e.g., as in *Hiroi and Pieters*, 1994], such that the imaginary index of refraction of a given mineral, k, can be inverted from its laboratory reflectance spectra acquired at a known grain size. Full methods are described in *Lapotre et al.* [2017]. To invert for the optical constants of our mineral endmembers, we used Hapke's theory following methods similar to those of *Lucey* [1998]. We assumed that sand grains are spherical with no internal porosity, scatter isotropically (phase function, $P = 1$) without backscattering (backscattering function, $B = 0$), and used the formulation of *Hapke* [1981] for the particle internal transmission coefficient. Uncertainties associated with the derivation of optical constants from reflectance spectra can be large, often due to uncertainties in grain size and grain-size distribution for particulate samples [e.g., *Poulet and Erard*, 2004]. Optical constant error quantification is outside of the scope of the present study because proper assessment of errors requires both reflectance and transmission data of all endmembers which is not available. Although our model outputs have uncertainties associated with the derivation of optical constants that remain unquantified, we attempted to minimize these by (i) selecting endmember spectra derived from laboratory samples with relatively narrow ranges in grain size (Table 1) and/or (ii) comparing our results to other published optical constants [e.g., *Lucey*, 1998; *Denevi et al.*, 2007; *Zeidler et al.*, 2011], such that we can assume that our input optical constants are reasonable estimates. The issue of the effects of uncertain optical constants on mixture modeling is examined further in a companion method-oriented paper [*Lapotre et al.*, 2017].

With the optical constants of endmember mineral phases on hand, the single-scattering albedo of a given mineral endmember can be calculated at the desired grain size, and then linear mixtures of those single-scattering albedos can be compared with the CRISM-derived single-scattering albedo to invert for both mineral abundances and grain sizes [*Mustard and Pieters*, 1987; *Poulet and Erard*, 2004; *Edwards and Ehlmann*, 2015; *Li and Milliken*, 2015; *Robertson et al.*, 2016]. Specifically, weight abundances and grain sizes of each endmember were sampled independently by our MCMC algorithm and then used together to compute the relative fractional geometric cross section of each mineral endmember. These were then used with optical constants to compute the modeled spectrum, which was compared with the CRISM single-scattering albedo spectrum.

We allowed for a covariance between data and model spectra of 2×10^{-4}, a value that we found (through trial and error) to appropriately account for noise in the single-scattering albedo-converted CRISM data (e.g., Figure 4). We allowed for grain sizes in the range of 50–800 μm for all mineral phases but magnetite, which we limited to a 10–200 μm range, due to the fact that it rarely occurs as large crystals in igneous systems. The chosen bounds bracket a range of grain sizes (silt to coarse sand) that is consistent with aeolian transport under Martian conditions [e.g., *Kok*, 2010a]. At each location, we inverted for a Markov chain of 10^6 models, i.e., 10^6 sets of mineral abundances and grain sizes matching the data within the allowed noise level.

In the following, we use three metrics to describe our results. The "maximum a posteriori probability" model, or "MAP," refers to the most sampled area of the parameter space, i.e., the most probable mineral assemblage. The MAP represents the mode of the 12-dimensional posterior (i.e., output) probability density

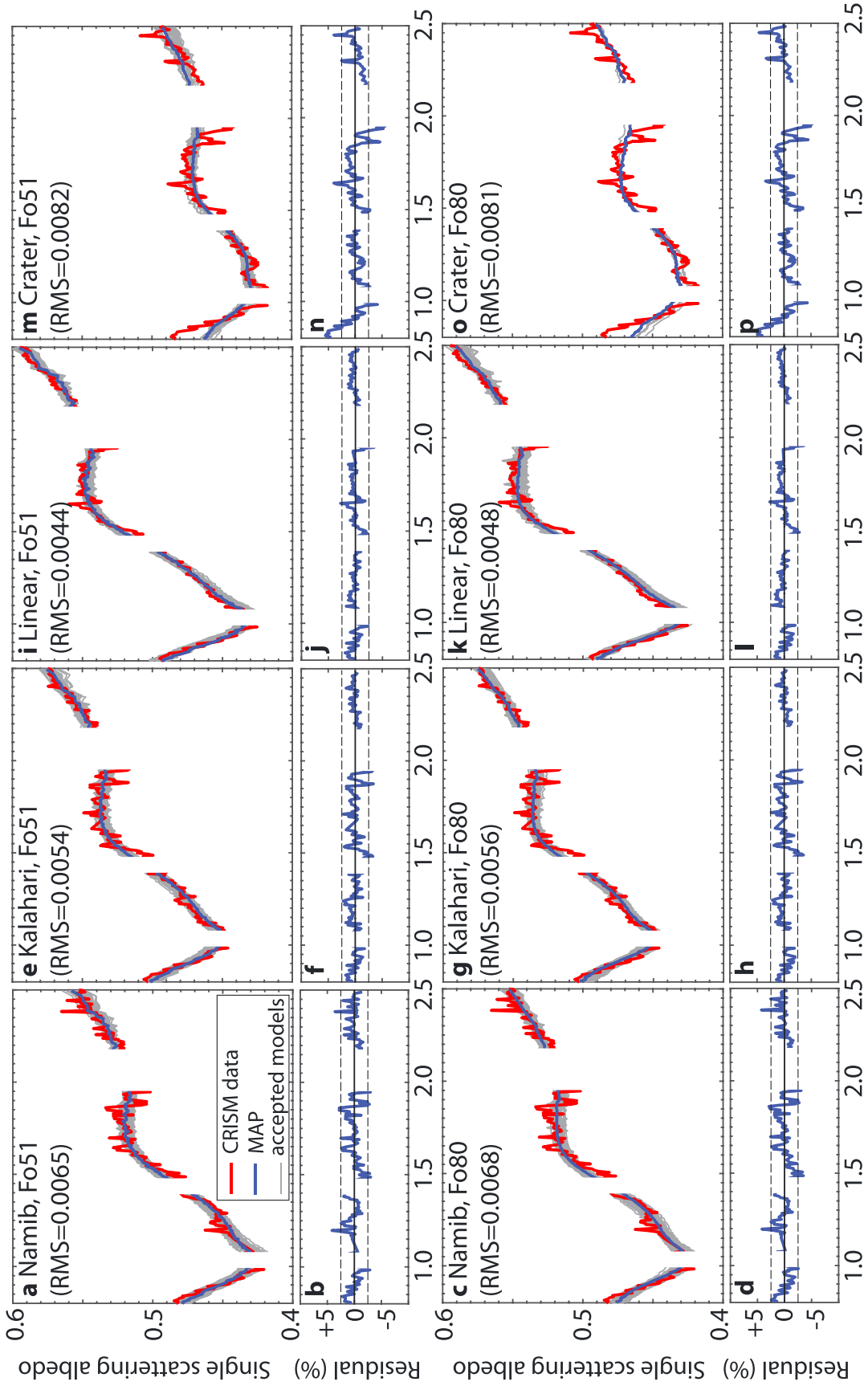

Figure 4. CRISM spectra (red), maximum a posteriori probability models (MAP; blue), and random subset of 1000 accepted models (gray) at (a) Namib Dune, (e) Kalahari Dune, (i) the linear dune, and (m) crater fill using an olivine of Fo51. (b, f, j, and n) Corresponding residuals of the MAP. The dashed lines represent a ±2.5% residual. CRISM spectra, MAPs, and random subset of 1000 accepted models at (c) Namib Dune, (g) Kalahari Dune, (k) the linear dune, and (o) crater fill using an olivine of Fo80, and (d, h, l, and p) corresponding residuals of the MAP. The dashed lines represent a ±2.5% residual.

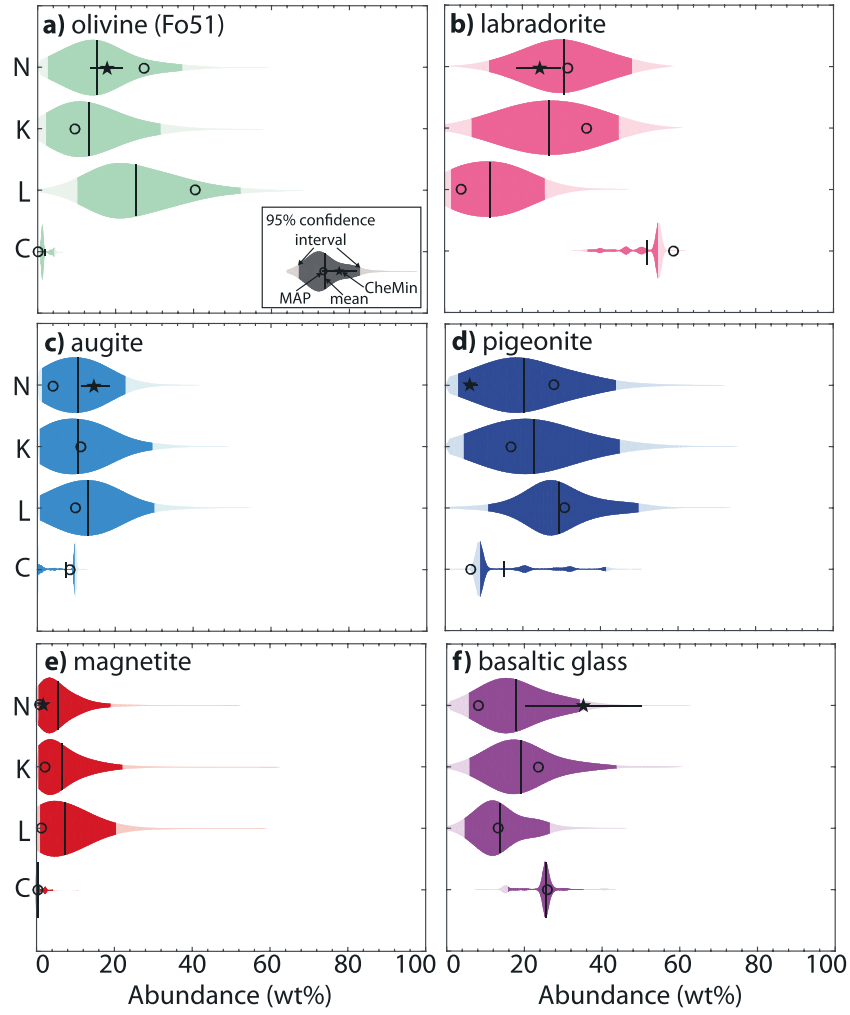

Figure 5. Probability densities of mineral abundances resulting from our Bayesian Hapke unmixing modeling using an olivine of Fo51 at the four locations of interest (N = Namib Dune; K = Kalahari Dune; L = linear dune; C = crater fill) for (a) olivine, (b) labradorite, (c) augite, (d) pigeonite, (e) magnetite, and (f) basaltic glass. The solid black lines indicate the mean model, while the open circles indicate the MAP. For Namib Dune, abundances inverted by CheMin in the <150 μm fraction (Table 4) were renormalized to our endmember phases only and are indicated by the filled stars. MAP values are summarized in Table 2.

function (six abundances and six grain sizes) and does not necessarily coincide with the mode of each individual parameter. The "mean" refers to the mean value of the parameter for all accepted models. Finally, the 95% confidence interval is defined as the centered bounds that contain 95% of all samples. Were the individual probability densities normally distributed, the 95% confidence interval would correspond to a $\pm 2\,\sigma$ interval around the mean.

3. Results

3.1. Properties of Sand Spectra

All spectra have broad ~1 μm and ~2 μm absorptions, indicative of the presence of olivine and pyroxenes. The main differences between the spectra in Figures 1c and 1d are (i) the strength of the olivine absorption at ~1 μm, (ii) the spectral continuum slope at the longer wavelengths, and (iii) the SWIR albedo at wavelengths great than ~1 μm. Stronger olivine absorptions, steeper SWIR continuum slopes, and higher SWIR albedos are observed in the barchans and the linear dunes compared with the crater fill. Stronger olivine signatures in select locations might suggest that olivine grains are more abundant and/or coarser in these locations, or that opaque dust does not deposit or is removed in more active areas due to stronger winds, or both.

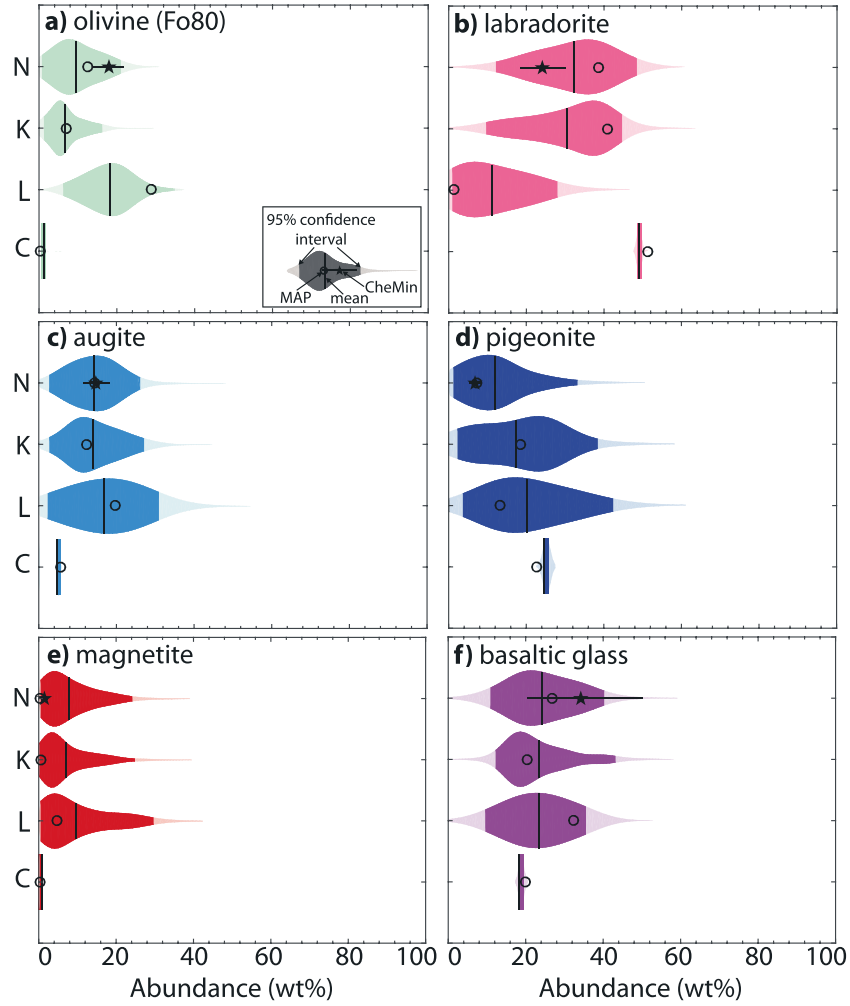

Figure 6. Probability densities of mineral abundances resulting from our Bayesian Hapke unmixing modeling using an olivine of Fo80 at the four locations of interest (N = Namib Dune; K = Kalahari Dune; L = linear dune; C = crater fill) for (a) olivine, (b) labradorite, (c) augite, (d) pigeonite, (e) magnetite, and (f) basaltic glass. The solid black lines indicate the mean model, while the open circles indicate the MAP. For Namib Dune, abundances inverted by CheMin in the <150 μm fraction (Table 4) were renormalized to our endmember phases only and are indicated by the filled stars. MAP values are summarized in Table 2.

3.2. Spatial Correlations Between Sand Flux, Composition, and Dust

We find that zones of high ripple displacements generally correspond to zones of higher OLINDEX3 and higher red/infrared ratios, e.g., at the Namib and Kalahari dunes (Figure 2). This spatial correlation may arise from (i) preferential enrichment of olivine where sand flux is higher and/or from (ii) the olivine signature being preferentially masked by dust in the less active parts of the dune field. Ferrous (Fe^{2+}) minerals tend to have higher red/infrared ratios than ferric (Fe^{3+}) phases like Martian dust. The observed correlation between OLINDEX3 and HiRISE red/infrared ratio suggests that dust content is lower where olivine abundance is high (Figures 2a and 2b). There is substantial scatter in the data of either index versus ripple displacement (Figures 2d and 2e). Nevertheless, we find that total ripple displacement is positively correlated with the binned mean of both the OLINDEX3 (Figure 2d) and the HiRISE red/infrared band ratio (Figure 2e) for those ripples that migrated less than about a ripple wavelength between the two consecutive HiRISE images.

Untangling the effects of mineral abundances, grain sizes, and dust cover from orbit remains difficult, and ground truth is required to definitively exclude the possibility that compositional variations merely indicate differences in masking of the primary mineralogy by dust. The Bagnold Dunes were previously determined to be generally dust-free [*Rogers and Bandfield*, 2009], are relatively active near the rover traverse

Table 2. MAP Abundances (in wt %) at Our Four Regions of Interest

	Namib		Kalahari		Linear		Crater	
	Fo51	Fo80	Fo51	Fo80	Fo51	Fo80	Fo51	Fo80
Olivine	27.3	12.6	9.5	7.1	40.5	29.0	0.2	0.4
Augite	4.0	14.3	11.2	12.3	9.9	19.7	8.3	5.6
Pigeonite	28.1	7.2	16.9	18.7	30.9	13.3	6.5	22.7
Labradorite	31.8	38.7	36.6	41.0	4.3	1.2	58.9	51.2
Magnetite	0.7	0.3	2.3	0.5	1.3	4.6	0.3	0.3
Basaltic glass	8.1	26.9	23.6	20.4	13.2	32.3	25.9	19.8

(e.g., Figure 2c) [*Silvestro et al.*, 2013, 2016; *Bridges et al.*, 2017; *Ewing et al.*, 2017] with dune displacements of about half those measured in the very active Nili Patera dune field [*Bridges et al.*, 2012], and HiRISE red/infrared band ratios are relatively high over the dunes (Figure 2b). In the following section, we quantitatively constrain the modal composition of bulk sands at four locations, assuming that the Bagnold sands are relatively dust-free (an assumption later discussed in section 4.2).

3.3. Quantifying Modal Mineralogy

Figure 4 shows the modeled MAP spectra (blue) at the four selected locations for two different olivine Fo numbers (Fo51 and Fo80), as well as a random subset of 1000 accepted models (gray). The spread in latter spectra illustrates the variability we allowed for through the covariance parameter. Associated residuals are typically less than 2.5%. Root-mean-square (RMS) errors of the MAPs are typically slightly higher for the Fo80 olivine inversions. For both olivine compositions, the crater fill (Figures 4m and 4o) displays a narrower range in accepted models (i.e., the gray lines are not as spread around the data spectra as for the other locations), which illustrates the fact that very few different models were acceptable according to our likelihood criterion, i.e., that most sampled models were deemed unlikely due to poor fits to the data. We interpret this result, along with the higher residuals, as reflecting a missing endmember in our parsimonious set, which we believe to most likely be fine dust. Indeed, fine ferric veneers over dark mafic materials, such as dust over dark basaltic sands, were shown to display spectral continuum slopes that are more "negative" than that of the underlying dark material alone [*Fischer and Pieters*, 1993], consistent with the observed lower spectral slope over the crater fill (Figure 1c).

Inverted mineral abundances are shown in Figures 5 and 6 for the Fo51 and Fo80 inversions, respectively. These figures are analogous to traditional box plots but with the shape of each box reflecting the probability density of a given parameter. Within each box, the area that is shaded in a darker hue outlines the 95% confidence interval of the corresponding parameter, while the vertical line and open circle indicate the mean and MAP, respectively. Table 2 summarizes the corresponding MAP abundances. Using a 95% confidence interval, inverted ranges in permitted abundances are wide, typically $>$30 wt %, but their probability densities tend to have distinct modes. With both olivine compositions, probability densities associated with the crater fill are much narrower than for the other locations, reflecting the low number of models deemed acceptable by our MCMC algorithm, and again, likely pointing to a missing component.

Inverted grain sizes are shown in Figures 7 and 8 for the Fo51 and Fo80 olivine compositions, respectively. It is important to note that inverted grain-size probability densities only reflect the range of sizes that yield satisfying fits to the data, not the true grain-size distributions on the ground. Table 3 summarizes the corresponding MAP grain sizes. In contrast to the probability densities of mineral abundances (Figures 5 and 6), those of grain sizes tend to lack well-defined modes. The overall uniformity of grain-size probability densities indicates the relative insensitivity of the inversion to grain size. In particular, mineral phases for which we find the mean model to be similar to the median of the allowed grain-size range (dashed line in Figures 7 and 8 at 425 μm for all phases but magnetite; 105 μm for magnetite) should be considered with caution. Interestingly, the basaltic glass seems to be required to be relatively fine-grained. Grain sizes of other mineral phases are more difficult to constrain from their roughly uniform probability densities, although the grain-size probability densities of olivine and pyroxenes appear to be consistently skewed toward relatively coarser and finer sizes, respectively.

Overall, the abundance and grain-size distributions are similar between the two tested Fo numbers. Olivine and plagioclase abundances are consistently spatially anticorrelated: olivine abundances decrease from the linear dune to Namib Dune, to Kalahari Dune, and to the crater fill, while plagioclase abundances decrease from the crater fill, to Kalahari Dune, to Namib Dune, and to the linear dune. All four locations appear to

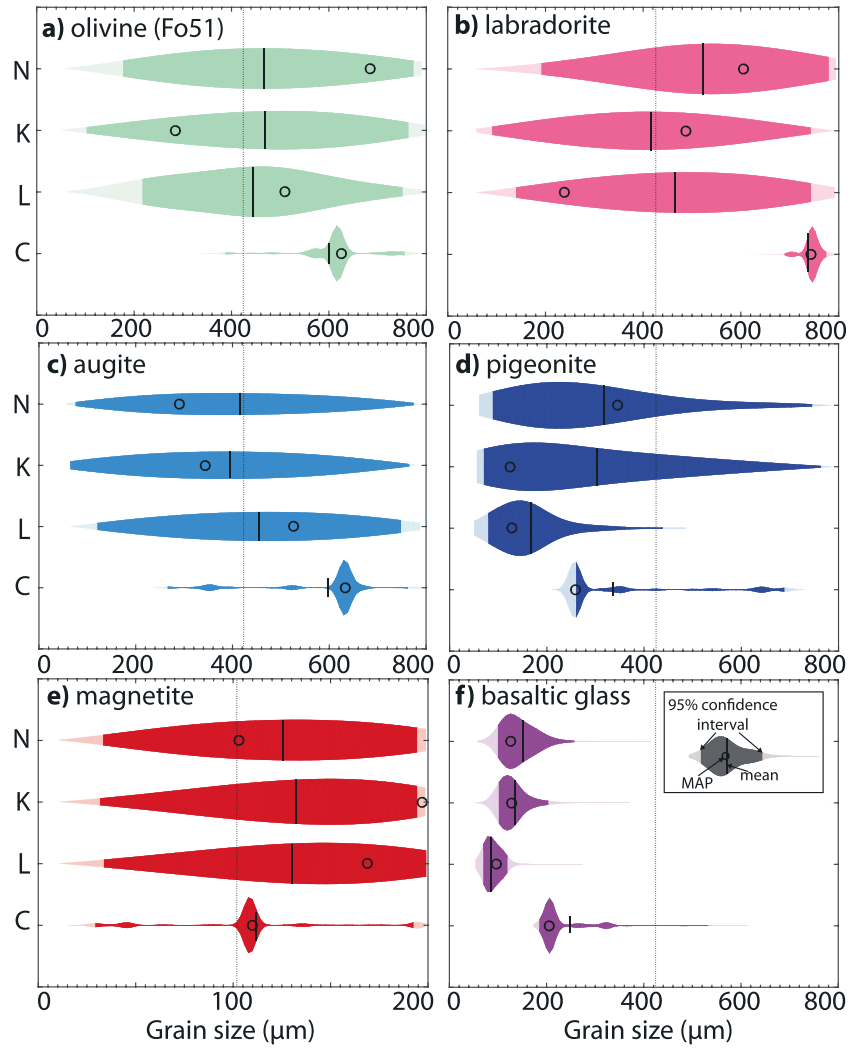

Figure 7. Probability densities of grain sizes resulting from our Bayesian Hapke unmixing modeling using an olivine of Fo51 at the four locations of interest (N = Namib Dune; K = Kalahari Dune; L = linear dune; C = crater fill) for (a) olivine, (b) labradorite, (c) augite, (d) pigeonite, (e) magnetite, and (f) basaltic glass. The solid black lines indicate the mean model, while the open circles indicate the MAP. The vertical dashed lines represent the median of the allowed grain-size range, i.e., the mean of a uniform grain-size distribution over that range. MAP values are summarized in Table 3.

have little magnetite (a few percent) and a significant fraction of basaltic glass. However, the spatial trends in pyroxene and basaltic glass abundances differ for the two Fo number cases.

4. Discussion

4.1. Evaluation of the Inversion Technique: Trade-Offs and Solid Solutions

Overall, our inversion technique produces many low RMS fits to spectra at three active sites. As discussed above, the small number of models with low RMS error for the crater-fill site is likely due to noninclusion of a dust layer on the relatively inactive bedforms. MCMC modeling of SWIR spectra successfully and quantitatively constrains the compositional range of the active sands, though this range is relatively broad, illustrating the inherent nonuniqueness of spectral inversions for basaltic materials. Retrieved plagioclase and magnetite abundances are relatively insensitive to olivine Fo number across sites, and this is likely because their retrieved abundances are governed largely by overall albedo. Additionally, the same trends in relative abundance by site are observed in olivine and plagioclase, regardless of the chosen Fo number. However, modeled abundances of other mafic minerals—augite, pigeonite, and basaltic glass—are affected by the olivine composition used in the model. A key contributor to this trade-off is the relative similarity of

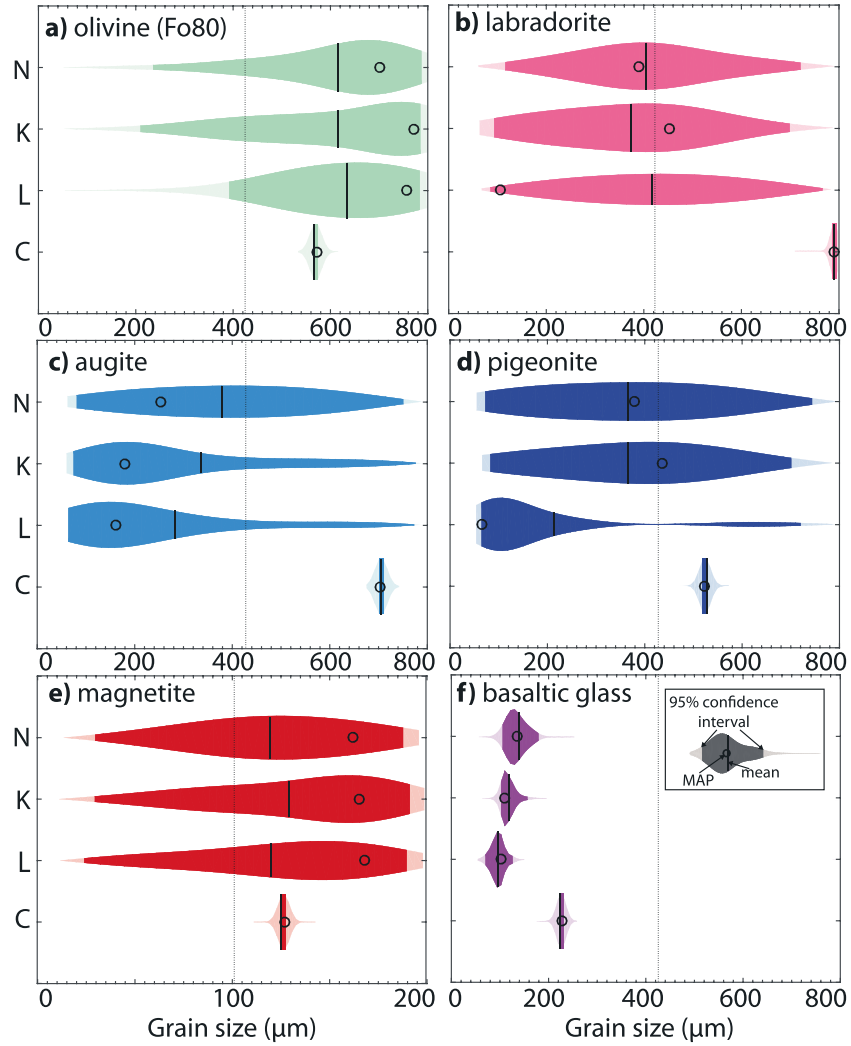

Figure 8. Probability densities of grain sizes resulting from our Bayesian Hapke unmixing modeling using an olivine of Fo80 at the four locations of interest (N = Namib Dune; K = Kalahari Dune; L = linear dune; C = crater fill) for (a) olivine, (b) labradorite, (c) augite, (d) pigeonite, (e) magnetite, and (f) basaltic glass. The solid black lines indicate the mean model, while the open circles indicate the MAP. The vertical dashed lines represent the median of the allowed grain-size range, i.e., the mean of a uniform grain-size distribution over that range. MAP values are summarized in Table 3.

absorption-feature shapes and locations in the different pyroxenes and basaltic glass. In particular, the position of their absorptions shifts continuously with solid-solution composition. There appear to be abundance-abundance trade-offs between endmembers and abundance-grain-size trade-offs within a single endmember in setting single-scattering albedo values. In particular, we suspect that the challenge

Table 3. MAP Grain Sizes (in μm) at Our Four Regions of Interest[a]

	Namib		Kalahari		Linear		Crater	
	Fo51	Fo80	Fo51	Fo80	Fo51	Fo80	Fo51	Fo80
Olivine	685	701	284	772	510	756	625	572
Augite	290	253	343	180	526	161	633	704
Pigeonite	345	378	125	436	128	66	259	522
Labradorite	606	390	487	452	239	106	744	790
Magnetite	103	162	197	165	169	168	110	127
Basaltic glass	127	135	129	110	96	102	205	228

[a]Note that for all phases but magnetite, a uniform distribution would have a mean grain size of 425 μm. For magnetite, a uniform distribution would have a mean of 105 μm.

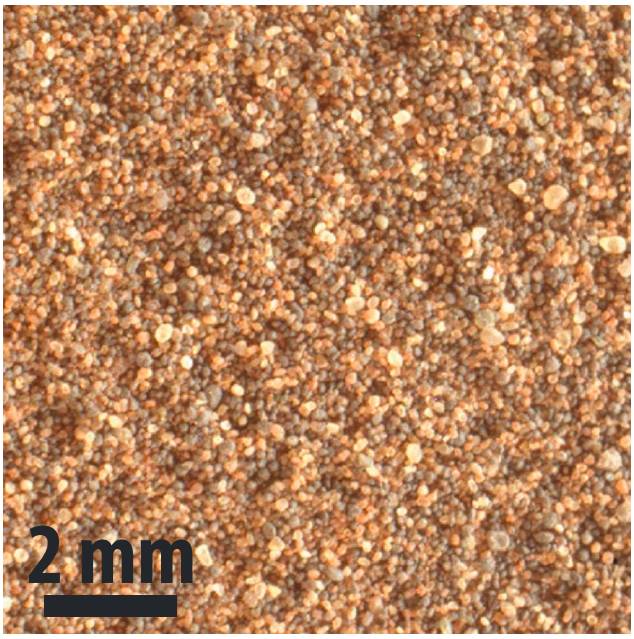

Figure 9. MAHLI focus merge product (1242MH0005740000403707R00) of the Otavi target, an undisturbed surface at the Gobabeb sampling site on Namib Dune.

of matching the precise shape of the 1 μm absorption (e.g., possibly due to an olivine Mg chemistry that differs slightly between the ground and our laboratory endmembers) is accommodated by trade-offs between olivine and basaltic glass abundances, which themselves impact the pyroxene abundances and the fit of the 2 μm feature. This caveat reflects the difficulty of inverting for mineral abundances when several solid solutions and/or an amorphous phase with similar spectral properties, in this cases two pyroxenes and mafic glasses, are present.

To summarize, potential sources of uncertainty in MCMC Hapke unmixing results for remote compositional analysis here and for the approach generally include (i) errors in model inputs, both for laboratory data (e.g., incorrect endmember suite and inaccuracies in optical constants) and in input orbiter-based data (e.g., instrumental noise and incomplete atmospheric correction); (ii) systematic errors in the forward model (e.g., in the physics and assumptions of the Hapke model formulation); and (iii) inherent nonuniqueness of the inverse problem (e.g., trade-offs between mineral abundances and grain sizes in setting single-scattering albedo values). A companion manuscript determines the relative importance of each of these parameters as sources of error and uncertainty [*Lapotre et al.*, 2017]. Here we evaluated the holistic performance of the MCMC Hapke modeling, as could be applied to any planetary surface, using ground truth data acquired by the Curiosity rover of mineralogy and grain size.

4.2. Comparison With In Situ Observations and Measurements From the Mars Science Laboratory Rover at Namib Dune

The Curiosity rover investigated the Namib Dune of the Bagnold Dune Field between Martian solar days (sols) ~1162 and ~1243 of the MSL mission [*Bridges and Ehlmann*, 2017]. In contrast to previous observations of loose regolith along the rover traverse, the Bagnold sands do not appear to contain intermixed dust and grains do not form clumps. The absence of dust is also confirmed by in situ compositional data sets [*Ehlmann et al.*, 2017; *Johnson et al.*, 2017; *O'Connell-Cooper et al.*, 2017]. The Mars Hand Lens Imager (MAHLI) documented that sand grains were very fine to medium in size, i.e., with most grains between 40 to 600 μm [*Ehlmann et al.*, 2017; *Edwards et al.*, 2017]. MAHLI data show that many sand grains appear to consist of individual mineral grains, although highly spherical dark grains could be lithics or beads of basalt or basaltic glass (Figure 9). Coarser particles are found on some surfaces near High Dune [*Ehlmann et al.*, 2017]. When sieved and discarded piles were examined, the coarse fractions (>150 μm) were found to have spectra, measured in situ, consistent with enrichment in olivine [*Johnson et al.*, 2017]. Additionally, chemical data from the Chemistry and Camera (ChemCam) and Alpha-Particle X-ray Spectrometer (APXS) data sets indicate that the coarse fraction has elevated MgO but lower SiO_2, Na_2O, and Al_2O compared with the finer fraction [*Cousin et al.*, 2017; *Ehlmann et al.*, 2017], though some quartz-feldspathic grains are also present (see also Figure 11a).

Mineral abundances were derived from the sieved fine fraction with the Chemistry and Mineralogy (CheMin) instrument, as summarized in *Achilles et al.* [2017] (see also Table 4). CheMin provides abundances at a high level of confidence for the crystalline phases in the <150 μm size fraction ingested by the instrument; however, abundance estimates of X-ray diffraction (XRD) amorphous phases are much less well constrained, such that uncertainty on absolute abundance of the crystalline phases remains relatively large. In Figures 5 and 6, the filled star symbols show mineral abundances measured by CheMin at Namib Dune, renormalized to the

Table 4. Weight Abundance of Mineral Endmembers of Interest as Measured by the CheMin Instrument Onboard Curiosity at Namib Dune [*Achilles et al.*, 2017][a]

Mineral Phases	Abundances (wt %)	Abundances Renormalized to Crystalline Phases Only (wt %)
Olivine (Fo ~55)	17.5	26.9
High-Ca pyroxene (Wo ~40)	14.9	22.9
Low-Ca pyroxene (Wo ~9)	7.1	11.0
Plagioclase (An ~63)	24.1	37.0
Magnetite	1.4	2.2
XRD amorphous	35.0	N/A

[a]Note that throughout this study, we compare our estimated abundance of basaltic glass to that of the XRD-amorphous phase, although the latter may also contain other phases. See *Achilles et al.* [2017] for raw data and associated uncertainties.

mineral phases we herein consider, with errors propagated to account for the large uncertainty on the XRD amorphous component. This amorphous component was estimated by combining CheMin and APXS data sets and found to represent 35 ± 15 wt % of the fine material at Namib Dunes [*Achilles et al.*, 2017] (Table 4).

Because in situ modal mineralogy was derived from the fine fraction only, and other ground-based images and compositional data sets show that chemistry varies with grain size and grain size varies between the ripples and interior of the dunes, we do expect some differences between CheMin abundances and our CRISM-based results, which reflect spatially averaged bulk sand mineralogy at the optical surface. However, we expect these differences to be relatively small, and CheMin abundances offer the opportunity to assess the performance of our inversion technique. CheMin abundances fall within our estimated 95% confidence intervals for all crystalline phases (Figures 5 and 6). The proportion of amorphous material measured in situ overlaps with our 95% confidence interval for the abundance of basaltic glass for both Fo numbers (see Namib abundances on Figures 5f and 6f). Average differences between the MAP and CheMin-derived abundances are 12.8 and 4.9 wt % for Fo51 and Fo80, respectively. Maximum errors are 14.6 wt % for the Fo80 case (labradorite) and 26.9 wt % for the Fo51 case (glass/XRD-amorphous, though this is somewhat uncertain because of the large uncertainties in the calculation of the XRD-amorphous component).

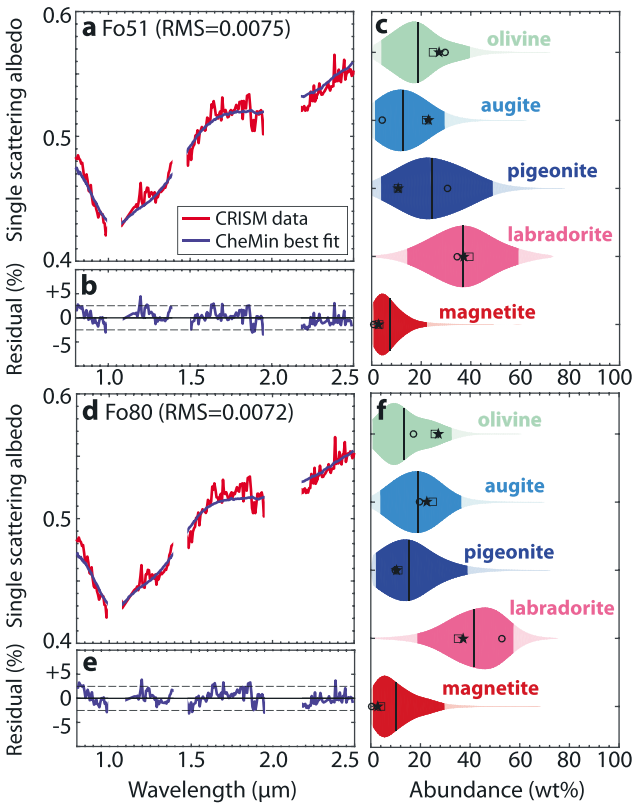

Figure 10. (a and d) CheMin best fit model (blue) compared with the Namib Dune single-scattering albedo using olivines of Fo51 and Fo80, respectively, and (b and e) corresponding residuals. The dashed lines represent ±2.5% residual. (c and f) Probability densities of mineral abundances resulting from our Bayesian Hapke unmixing modeling at Namib Dune using olivines of Fo51 and Fo80, respectively, renormalized to crystalline phases only. The solid black lines indicate the mean model, while the open circles indicate the MAP, and the open squares indicate the inverse model that best approaches CheMin inferences (herein referred to as "CheMin best fit").

Figure 10c also shows a comparison between the CheMin data (filled star) and the MAP (open circle), renormalized to crystalline phases only (i.e., without the basaltic glass). Average differences between the MAP and CheMin-derived abundances are 9.0 and 6.3 wt % for

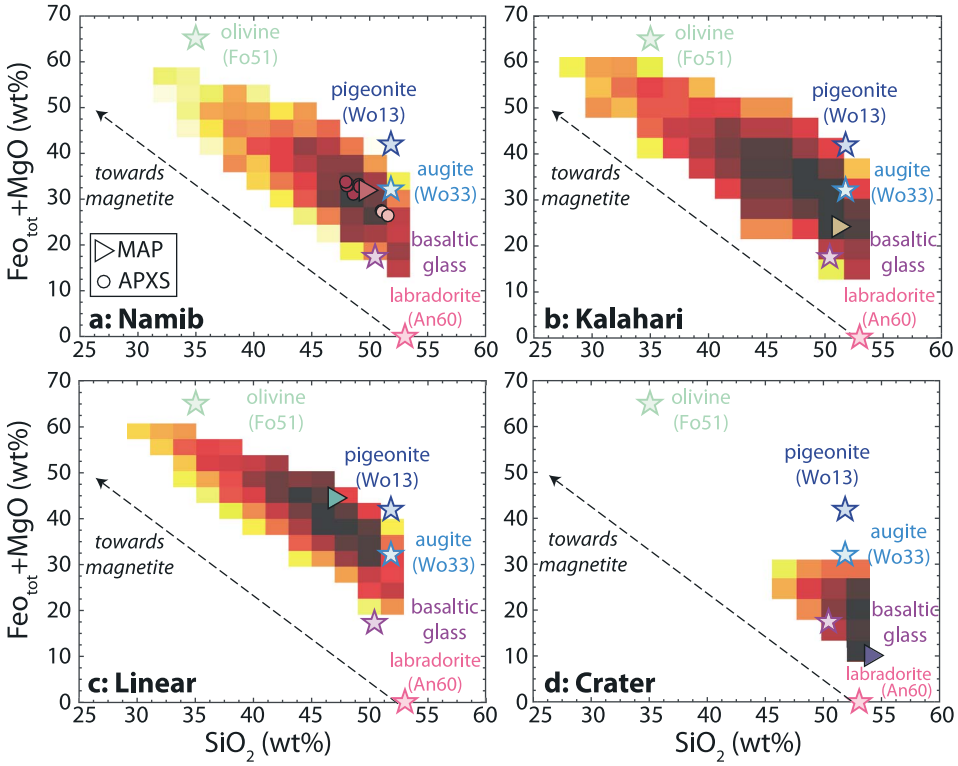

Figure 11. Estimated FeO_{tot} + MgO versus SiO_2 of all accepted samples (heat map), the MAP (triangle), and mineral endmemebers (stars) at (a) Namib Dune, (b) Kalahari Dune, (c) the linear dune, and (d) the crater fill. Assumptions used to convert mineralogy to oxides abundances are described in section 4.2. Heat map reflects the density of accepted samples, with darker colors indicating more densely sampled regions. At Namib Dune, the circles indicate APXS measurements, which appear to cluster into two groups—the coarser (more mafic; darker circles) and the finer (more felsic; pale circles) samples. Note that for a direct comparison with our estimates from CRISM, the APXS oxide weight abundances were renormalized to the main seven oxides (SiO_2, Al_2O_3, CaO, FeO, MgO, Na_2O, and K_2O).

Fo51 and Fo80, respectively. Maximum errors are 19.7 wt % for Fo51 (pigeonite) and 15.9 wt % for Fo80 (labradorite). Inverted abundances using an olivine of Fo51 are very close to those measured by CheMin for olivine, plagioclase, and magnetite. The sum of the pigeonite and augite is also close to ground truth, although the relative abundances of low and high Ca pyroxenes are not well estimated. When pyroxenes are combined into "total pyroxene," the mean error of the MAP abundances drops to 1.9 wt %, with a maximum error of 2.8 wt % for olivine. Conversely, the pyroxene abundances and relative proportions appear to be well estimated in our inversion with an olivine of Fo80, but olivine and plagioclase are not as well predicted. For both Fo numbers, the discrepancies between our results and in situ measurements most likely arise from trade-offs between the abundances and grain sizes of our mineral endmembers further complicated by mineral endmember that are not exactly chemically representative of the precise solid solutions on the ground (Table 4).

In order to illustrate the usefulness of the Bayesian approach, we identified the accepted model with modeled mineral abundances most closely matching the mineral abundances obtained from CheMin (herein referred to as the CheMin best fit; Figures 10c and 10f, open squares). Figures 10a, 10b, 10d, and 10e show a comparison between the modeled spectrum from the CheMin best fit and the CRISM single-scattering albedo data. Interestingly, the RMS errors for the CheMin best fit are 0.0075 and 0.0072 for Fo51 and Fo80, respectively, and are higher than that of the corresponding MAPs (RMS errors of 0.0065 and 0.0068 for Fo51 and Fo81, respectively; Figures 4a and 4c); this confirms that a simple error minimization algorithm would have missed the true composition under the model and assumptions presented here.

While the RMS errors between CRISM and model spectra are generally lower when using the Fo51 olivine, the aforementioned trade-offs between solid solutions prevent a confident estimate of olivine chemistry from the VSWIR data alone. However, CheMin measurements suggest an olivine of intermediate Mg content,

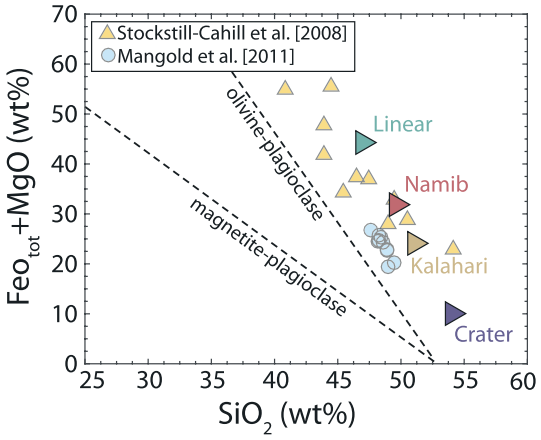

Figure 12. Comparison between our estimated MAP SiO_2 and FeO_{tot} + MgO compositions at the four sites and observed compositional variations in basaltic sands in Iceland on Earth (blue circles [*Mangold et al.*, 2011]) and Amazonis Planitia on Mars (orange triangles [*Stockstill-Cahill et al.*, 2008]).

with an estimated Fo of 55 [*Achilles et al.*, 2017]. We hypothesize that the discrepancy in pyroxene chemistry between our Fo51 scenario and ground truth arises from trade-offs between the pyroxene phases and the basaltic glass in an attempt to fit the 1 μm absorption, whose breadth and position are determined by the Fo number of the olivine. However, the relative proportions of crystalline phases are well constrained from CRISM when high- and low-Ca pyroxenes are summed and considered as total pyroxene. In the following section, we discuss the implications of our inverted mineral compositions for aeolian processes at Gale crater based on our Fo51 scenario.

4.3. Implications for Sorting, Transport Distances, and Sand Sources Within the Bagnold Dune Field

The most readily visible compositional variation from VSWIR orbital data within the Bagnold Dunes of Gale crater is that of the mafic phases, in particular the relative enrichment of the barchan dunes in olivine on the upwind, or trailing, margin of the dune field [*Seelos et al.*, 2014] (see also Figure 1b). Unmixing results show that olivine and plagioclase abundances are anticorrelated at the four locations we investigated (section 3.2), a trend qualitatively consistent with previous studies of aeolian basaltic sands, which showed that wind sorting tends to segregate felsic and mafic phases on Earth and Mars [*Stockstill-Cahill et al.*, 2008; *Mangold et al.*, 2011]. *Fedo et al.* [2015] suggested that the observed segregation of mafic and felsic minerals in nonchemically weathered basaltic sands of Earth and Mars is primarily controlled by the distribution of phenocrysts in the parent rock, and subsequent sorting of those grains [e.g., *Nesbitt and Young*, 1996; *Fralick*, 2003; *Mangold et al.*, 2011]. The modes and dynamics of sediment transport are dictated by grain densities, sizes, and shapes, which generate feedback that govern grain sorting [e.g., *Mason and Folk*, 1958; *Parfenoff et al.*, 1970; *Hunter and Richmond*, 1983; *Anderson and Bunas*, 1993; *Makse*, 2000]. In particular, *Mangold et al.* [2011] showed that windblown basaltic sands in Iceland were enriched in mafic phases as transport distance increases.

To quantitatively compare our results with those of *Mangold et al.* [2011], who only report chemical data, we convert our inverted mineral compositions into oxide abundances. In order to do so, we assume (i) that solid solutions are at thermodynamic equilibrium; (ii) a Fo number of 51 for the olivine; (ii) wollastonite (Wo) numbers of 13 and 33 for the pigeonite and augite, respectively; (iii) an anorthite number (An) of 60 for the plagioclase; and (iv) a composition of the basaltic glass as that of our laboratory basaltic glass (~50.4 wt % SiO_2 and ~17.5 wt % FeO_{tot} + MgO). Use of assumed chemical compositions reflects our approach not to use data only obtainable by Curiosity. We also conducted the same analysis with the CheMin-derived compositions (Table 4), which did not alter the trends.

In (SiO_2, FeO_{tot} + MgO) space for the four locations (Figure 11), estimated compositions for our accepted models (heat map) are spread parallel to the plagioclase-magnetite join, reflecting the primary trade-off of mixing bright and dark minerals to match the overall albedo of the data. However, the most densely populated region in this oxides space (darker colors in the heat map) plots in a triangle between the plagioclase-olivine join and pyroxenes, and all MAPs plot within this region. At Namib Dune (Figure 11a), we compare our estimates to oxide abundances measured by the APXS instrument. APXS data mostly fall into two clusters—coarser samples (darker circles) having elevated Fe and Mg and lower Si than the finer samples (pale circles)—which both fall within the most-densely populated region above the plagioclase-olivine join. Our inverted MAP at Namib Dune is close to the APXS cluster of coarser samples in this space [*Ehlmann et al.*, 2017; *O'Connell-Cooper et al.*, 2017]. The MAP results for the four locations (Figure 12) do not trend along the

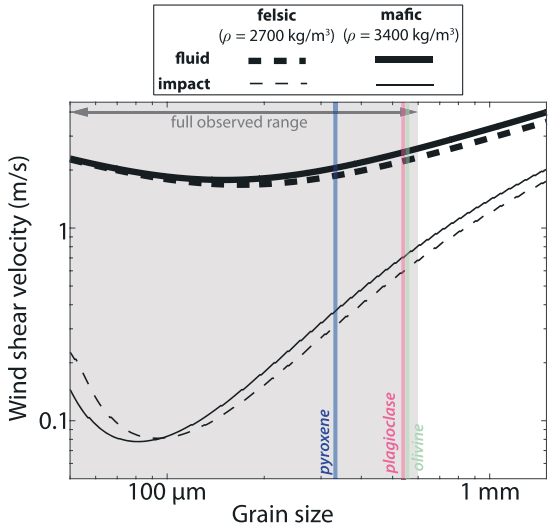

Figure 13. Wind shear velocities required to initiate (thick lines) and sustain (thin lines) transport of the inferred grain sizes for olivine (530 µm; green), pyroxene (310 µm; blue), and plagioclase (520 µm; magenta), as estimated from our Fo51 inversion results. Wind shear velocities were estimated from the formulations of *Shao and Lu* [2000] and *Kok* [2010b]. The light gray box outlines the full range of grain sizes observed with MAHLI [*Ehlmann et al.*, 2017].

plagioclase-magnetite join but rather parallel a plagioclase-olivine join in a trend most similar to that of the sand deposits of *Stockstill-Cahill et al.* [2008] (dark intracrater sand deposits in Amazonis Planitia, Mars) and *Mangold et al.* [2011] (nonchemically weathered volcanic sand in Iceland). The latter compositional spread is consistent with sorting and/or mixing of minerals grains.

Sorting of mineral grains by the wind likely contributes to compositional and grain-size variability observed from orbit (Figure 1b) and by the rover (section 4.2). Indeed, the wind speed required to initiate saltation of sand particles, often parametrized as fluid threshold shear velocity, is a function of grain density, size, and shape [*Bagnold*, 1941; *Shao and Lu*, 2000]. The threshold wind speed to maintain saltation, or impact threshold shear velocity, can be over an order of magnitude lower than the fluid threshold because of the effect of low atmospheric density on saltation trajectories and kinetics [*Kok*, 2010a]. This difference leads to a hysteresis in sand transport, such that winds required to sustain transport are much weaker than those required to initiate it. On Earth, impact and fluid thresholds are more similar [*Kok et al.*, 2012], such that the transport hysteresis is comparatively weak. On Mars, the strong dependence of the impact threshold on grain size suggests that winds below the fluid threshold may be very efficient at size-sorting sand grains.

Dune-forming wind speeds can be estimated from grain densities and sizes under the assumption of spherical grains, though this is an approximation. Based on an air temperature of 225 K and an atmospheric pressure of 6 mbar at Gale crater [e.g., *Haberle et al.*, 2014], we calculate both thresholds for transport under Martian conditions from the semiempirical formulations of *Shao and Lu* [2000] and *Kok* [2010b], which were developed for unimodal grain-size distributions. In reality, bed grain-size distributions have a finite width (very fine to medium sand [*Ehlmann et al.*, 2017]), such that the threshold models we employ may be viewed as reasonable approximations. We find that grain size is more important than density in determining thresholds of motion for the phases herein considered (Figure 13).

For the average MAP grain sizes of olivine (~530 µm), bulk pyroxenes (~310 µm), and plagioclase (~520 µm), the required wind speeds to sustain transport of the coarser olivine grains (~0.70 m/s) are about twice those required to sustain transport of the pyroxene grains (~0.34 m/s) and ~25% larger than those required to sustain transport of plagioclase grains (~0.58 m/s). Conversely, the wind speeds required to initiate saltation of all mineral grains are more similar (between ~2.0 and 2.5 m/s). Following the premise that dune-forming winds may be constrained from the size of grains that are barely saltatable [e.g., *Fenton et al.*, 2016], we infer that dune-forming wind shear velocities at the Bagnold Dunes are typically at least 0.4–0.7 m/s with excursions upward of 2.5 m/s. Indeed, if wind speeds were always lower than the fluid threshold, coarse olivine grains could not be transported in saltation at all, while if typical wind speeds were higher than the fluid threshold, coarse olivine grains would be effectively transported across the entire dune field (along with pyroxene grains). While our CRISM-based grain-size estimates tend to be on the higher end of sizes observed on the ground, our wind-shear velocity extrapolations are consistent with Rover Environmental Monitoring Station measurements (REMS) during the Martian low-sand flux season (~0.1–0.3 m/s [*Newman et al.*, 2017]) and are consistent with shear velocities inferred from global circulation models and regional studies (0.71–1.22 m/s, assuming an atmospheric density of 0.02 kg/m^3) [*Haberle et al.*, 2003; *Ayoub et al.*, 2014].

In addition to wind-sorting, mixing sediments from two sources would also spread the compositional data parallel to the plagioclase-olivine join. The magnitude of the spread in chemical composition we invert for at our four sites dwarfs that observed by *Mangold et al.* [2011] in Iceland, despite being measured over an order-of-magnitude shorter length scale (few versus tens of kilometers), but is similar to that estimated by *Stockstill-Cahill et al.* [2008] in Amazonis Planitia over >2000 km. It thus seems unlikely that wind-sorting alone could explain such a large compositional spread as what we infer for the Bagnold Dunes, and we hypothesize that the dune field may be replenished in plagioclase from a more proximal sand source. Indeed, the active dunes might be eroding bedrock and incorporating eroded material. MAHLI images of sands near High Dune show sparse but clear evidence for input from local sediment sources (e.g., coarse and irregular bright grains [see *Ehlmann et al.*, 2017]). More in situ data, such as from the linear dunes to the south of Namib Dune, would allow us to further test this hypothesis. Potential sources include eroded and transported olivine-bearing materials from Gale crater's walls [*Ehlmann and Buz*, 2015] and more local, perhaps more felsic materials, possibly present in the walls too, but certainly present in the coarse-grained conglomerates of Aeolis Palus [*Sautter et al.*, 2015].

4.4. Implications for the Interpretation of Martian Aeolian Sandstones

Aeolian sandstones reflect the compositional and grain-size variations within the dune field from which they formed. On Earth, most aeolian sandstones are relatively homogeneous because of the strong sorting effects of wind, and because most large aeolian deposits arise from extensive fluvial and coastal systems, which preferentially sort sand grains prior to the formation of a dune field. Indeed, in well-connected transport pathways, grains of varying mineralogy and sizes are sorted over long transport distances, resulting in homogenous materials in dune fields. Examples include many large aeolian systems, such as the deserts of China, the Middle East, and Africa. In some cases, the compositional and grain-size variations of aeolian dune fields may be high where the source area is nearby and the transport out of the basin is limited [e.g., *Fenton et al.*, 2016], though this type of system only represents a small part of the overall terrestrial aeolian rock record. In addition to sorting, efficient surface weathering can select for the most prevalent and resistant minerals on Earth, such as quartz and potassium feldspar, which make up most of Earth's aeolian sandstones. On Mars, however, the formation of aeolian sand and the accumulation and preservation of aeolian sandstones is relatively poorly understood [e.g., *Kocurek and Ewing*, 2012], but our results suggest that primary variations of ~7 wt % in SiO_2 and ~20 wt % in FeO_{tot} + MgO may arise over a length scale of a few kilometers only from sorting of basaltic sand and/or mixing well-sorted sand with local sediment sources. If the Bagnold Dunes of Gale crater are representative of the sediments forming aeolian sandstones on Mars, Martian aeolian sandstones may be more poorly sorted and compositionally diverse than terrestrial aeolian sandstones. Martian sandstones [e.g., *Grotzinger et al.*, 2005; *Milliken et al.*, 2014; *Banham et al.*, 2016] thus offer the opportunity to characterize ancient aeolian environments and sediment sources if the physical sorting effects on bulk chemistry can be disentangled from chemical changes due to diagenesis and later alteration.

5. Conclusions

Spectral variability, in particular in the signature of mafic minerals, is readily observable from CRISM data over the Bagnold Dune Field at Gale crater. We showed that there is a qualitative correlation between zones of stronger olivine signatures, inferred lower dust cover, and higher sand fluxes. Under the assumption that dust cover is minor within the active dunes, we invert for modal mineralogy and grain sizes of the sands from CRISM shortwave infrared spectra at four locations near the traverse of the Curiosity rover from a Bayesian implementation of the Hapke radiative transfer model. Between sols ~1162 and ~1243, the Curiosity rover investigated the Bagnold Dunes at Gale crater, offering an unprecedented opportunity to test our orbiter-based predictions against in situ measurements of mineral composition and grain sizes. Our quantitative estimates of bulk mineralogy favorably compare with in situ measurements from the CheMin instrument onboard Curiosity at the Namib Dune sampling site, with an average error of ~9 wt % for crystalline endmembers. Our inversion technique and subsequent comparison with in situ data sets illustrate the difficulty in resolving the precise chemistry of solid solutions on the ground due to spectral trade-offs between mineral endmembers and grain sizes. However, model results suggest that observed spectral variations within the dune field arise from anticorrelated abundances of olivine and plagioclase grains. Our results are consistent with sorting of the grains during aeolian transport, and in particular with the Earth-based observation that

winds tend to segregate mafic and felsic phases. In addition, we hypothesize that multiple sand sources of contrasting compositions may be mixing at the Bagnold Dunes. Altogether, our quantitative constraints provide a guide for the interpretation of both modern and ancient aeolian environments on Mars from measurements of the chemical and mineral compositions of sands.

Acknowledgments
We are indebted to the MSL Engineering and Science and Operations teams for collecting the in situ data, and Chi Ma of Caltech for compositional measurements of our basaltic-glass sample. We thank Alan Delamere and Rodney Heyd for their guidance on the use of HiRISE band ratios, and Christopher Edwards for providing us with the seamless color HiRISE mosaic shown in Figure 1a. Thanks to the CRISM Operations team for collecting the data set and to the CheMin team for rapid sharing of their results from MSL analyses on Mars. We also thank Tim Titus and Jessica Ball of the U.S. Geological Survey for informal reviews of our manuscript and Ralph Milliken and an anonymous reviewer for thorough reviews that improved our original manuscript. A portion of this research was carried out at the Jet Propulsion Laboratory, California Institute of Technology, under a contract with the National Aeronautics and Space Administration. M.G.A.L. was partially funded by a NASA Earth and Space Science Fellowship (12-PLANET12F-0071) and from a MSL participating Scientist Program grant to B.L.E. A.A.F. also acknowledges funding from a MSL Participating Scientist Program grant. Data presented in this paper is or will be posted on the Planetary Data System (PDS).

References

Achilles, C. N., et al. (2017), Mineralogy of an active eolian sediment from the Namib dune, Gale crater Mars, *J. Geophys. Res. Planets*, *122*, doi:10.1002/2017JE005262.

Anderson, R., and J. Bell III (2010), Geologic mapping and characterization of Gale crater and implications for its potential as a Mars Science Laboratory site, *Mars*, *5*, 76–128, doi:10.1555/mars.2010.0004.

Anderson, R. S., and K. L. Bunas (1993), Grain size segregation and stratigraphy in aeolian ripples modelled with a cellular automaton, *Nature*, *365*(6448), 740–743.

Arvidson, R., S. Squyres, J. Bell, J. Catalano, B. Clark, L. Crumpler, P. de Souza, A. Fairen, W. Farrand, and V. Fox (2014), Ancient aqueous environments at Endeavour crater, Mars, *Science*, *343*(6169), 1248097, doi:10.1126/science.1248097.

Arvidson, R., et al. (2015), Mars Reconnaissance Orbiter and Opportunity observations of the Burns formation: Crater hopping at Meridiani Planum, *J. Geophys. Res. Planets*, *120*, 429–451, doi:10.1002/2014JE004686.

Ayoub, F., J.-P. Avouac, C. Newman, M. Richardson, A. Lucas, S. Leprince, and N. Bridges (2014), Threshold for sand mobility on Mars calibrated from seasonal variations of sand flux, *Nat. Commun.*, *5*, 5096, doi:10.1038/ncomms6096.

Bagnold, R. A. (1941), The physics of wind blown sand and desert dunes, *Methuen, London*, *265*.

Banham, S. S., S. Gupta, D. M. Rubin, J. A. Watkins, D. Y. Sumner, J. P. Grotzinger, K. W. Lewis, K. S. Edgett, L. A. Edgar, and K. M. Stack (2016), Reconstruction of an ancient eolian dune field at Gale crater, mars: Sedimentary analysis of the Stimson formation, in *Proc. Lunar Planet. Sci. Conf. 47th*, 2346 pp., Woodlands, Tex.

Bridges, N. T., and B. L. Ehlmann (2017), The Mars Science Laboratory (MSL) Bagnold Dunes campaign, Phase I: Overview and introduction to the special issue, *J. Geophys. Res. Planets*, *122*, doi:10.1002/2017JE005401.

Bridges, N. T., et al. (2017), Martian aeolian activity at the Bagnold Dunes, Gale crater: The view from the surface and orbit, *J. Geophys. Res. Planets*, *122*, doi:10.1002/2017JE005263.

Bridges, N., F. Ayoub, J. Avouac, S. Leprince, A. Lucas, and S. Mattson (2012), Earth-like sand fluxes on Mars, *Nature*, *485*(7398), 339–342, doi:10.1038/nature11022.

Bridges, N., F. Calef, B. Hallet, K. Herkenhoff, N. Lanza, S. Le Mouelic, C. Newman, D. Blaney, M. Pablo, and G. Kocurek (2014), The rock abrasion record at Gale crater: Mars Science Laboratory results from Bradbury landing to Rocknest, *J. Geophys. Res. Planets*, *119*, 1374–1389, doi:10.1002/2013JE004579.

Chojnacki, M., D. Burr, and J. Moersch (2013), Local sourcing and aeolian fractionation as factors for compositional heterogeneity of Martian aeolian bedform sand, *Proc. Lunar Planet. Sci. Conf. 44th*, 3031 pp., Woodlands, Tex.

Clark, R. N., G. A. Swayze, R. Wise, K. E. Livo, T. M. Hoefen, R. F. Kokaly, and S. J. Sutley (2007), *USGS Digital Spectral Library splib06a*, U.S. Geol. Surv., Reston, Va. [Available at https://speclab.cr.usgs.gov/spectral.lib06/.]

Cousin, A., et al. (2017), Geochemistry of the Bagnold Dune Field as observed by ChemCam, and comparison with other aeolian deposits at Gale crater, *J. Geophys. Res. Planets*, *122*, doi:10.1002/2017JE005261.

Day, M., and G. Kocurek (2016), Observations of an aeolian landscape: From surface to orbit in Gale crater, *Icarus*, *280*, 37–71, doi:10.1016/j.icarus.2015.09.042.

Day, M., W. Anderson, G. Kocurek, and D. Mohrig (2016), Carving intracrater layered deposits with wind on Mars, *Geophys. Res. Lett.*, *43*, 2473–2479, doi:10.1002/2016GL068011.

Denevi, B. W., P. G. Lucey, E. J. Hochberg, and D. Steutel (2007), Near-infrared optical constants of pyroxene as a function of iron and calcium content, *J. Geophys. Res.*, *112*, E05009, doi:10.1029/2006JE002802.

Delamere, W. A., L. L. Tornabene, A. S. McEwen, K. Becker, J. W. Bergstrom, N. T. Bridges, E. M. Eliason, D. Gallagher, K. E. Herkenhoff, and L. Keszthelyi (2010), Color imaging of Mars by the High Resolution Imaging Science Experiment (HiRISE), *Icarus*, *205*(1), 38–52, doi:10.1016/j.icarus.2009.03.012.

Edwards, C. S., and B. L. Ehlmann (2015), Carbon sequestration on Mars, *Geology*, *43*(10), 863–866, doi:10.1130/G36983.1.

Edwards, C. S., S. Piqueux, V. E. Hamilton, R. L. Fergason, K. E. Herkenhoff, A. R. Vasavada, L. Sacks, K. Lewis, and M. D. Smith (2017), The thermophysical properties of the Bagnold Dunes, Mars: Ground-truthing orbital data, http://arxiv.org/abs/1711.10699.

Ehlmann, B. L., and J. Buz (2015), Mineralogy and fluvial history of the watersheds of Gale, Knobel, and Sharp craters: A regional context for the Mars Science Laboratory Curiosity's exploration, *Geophys. Res. Lett.*, *42*, 264–273, doi:10.1002/2014GL062553.

Ehlmann, B. L., et al. (2017), Chemistry, mineralogy, and grain properties at Namib and high dunes, Bagnold Dune Field, Gale crater, Mars: A synthesis of Curiosity rover observations, *J. Geophys. Res. Planets*, *122*, doi:10.1002/2017JE005267.

Ewing, R. C., et al. (2017), Sedimentary processes of the Bagnold Dunes: Implications for the eolian rock record of Mars, *J. Geophys. Res. Planets*, *122*, doi:10.1002/2017JE005324.

Fedo, C. M., I. O. McGlynn, and H. Y. McSween (2015), Grain size and hydrodynamic sorting controls on the composition of basaltic sediments: Implications for interpreting martian soils, *Earth Planet. Sci. Lett.*, *423*, 67–77, doi:10.1016/j.epsl.2015.03.052.

Fenton, L. K., J. L. Bishop, S. King, B. Lafuente, B. Horgan, D. Bustos, and P. Sarrazin (2016), Sedimentary differentiation of aeolian grains at the White Sands National Monument, New Mexico, USA, *Aeolian Res.*, doi:10.1016/j.aeolia.2016.05.001.

Fischer, E. M., and C. M. Pieters (1993), The continuum slope of Mars: Bidirectional reflectance investigations and applications to Olympus Mons, *Icarus*, *102*(2), 185–202.

Fralick, P. W. (2003), Geochemistry of clastic sedimentary rocks: Ratio techniques, in *Geochemistry of Sediments and Sedimentary Rocks, Geotext*, vol. 4, edited by D. R. Lentz, pp. 85–104, Geol. Assoc. of Canada, Toronto, Canada.

Grotzinger, J. P., R. Arvidson, J. Bell, W. Calvin, B. Clark, D. Fike, M. Golombek, R. Greeley, A. Haldemann, and K. Herkenhoff (2005), Stratigraphy and sedimentology of a dry to wet eolian depositional system, Burns formation, Meridiani Planum, Mars, *Earth Planet. Sci. Lett.*, *240*(1), 11–72, doi:10.1016/j.epsl.2005.09.039.

Haberle, R., J. Gomez-Elvira, M. Torre Juarez, A. M. Harri, J. Hollingsworth, H. Kahanpaa, M. Kahre, M. Lemmon, F. Martin-Torres, and M. Mischna (2014), Preliminary interpretation of the REMS pressure data from the first 100 sols of the MSL mission, *J. Geophys. Res. Planets*, *119*, 440–453, doi:10.1002/2013JE004488.

Haberle, R. M., J. R. Murphy, and J. Schaeffer (2003), Orbital change experiments with a Mars general circulation model, *Icarus*, *161*(1), 66–89, doi:10.1016/S0019-1035(02)00017-9.
Hapke, B. (1981), Bidirectional reflectance spectroscopy: 1. Theory, *J. Geophys. Res.*, *86*(B4), 3039–3054.
Hiroi, T., and C. M. Pieters (1994), Estimation of grain sizes and mixing ratios of fine powder mixtures of common geologic minerals, *J. Geophys. Res.*, *99*(E5), 10867–10879.
Hobbs, S. W., D. J. Paull, and M. C. Bourke (2010), Aeolian processes and dune morphology in Gale crater, *Icarus*, *210*(1), 102–115, doi:10.1016/j.icarus.2010.06.006.
Hunter, R. E., and B. M. Richmond (1983), Storm-controlled oblique dunes of the Oregon coast, *Geol. Soc. Am. Bull.*, *94*(12), 1450–1465.
Johnson, J. R., W. M. Grundy, M. T. Lemmon, J. F. Bell III, M. J. Johnson, R. Deen, R. Arvidson, W. Farrand, E. Guinness, and A. G. Hayes (2006a), Spectrophotometric properties of materials observed by Pancam on the Mars Exploration Rovers: 2. Opportunity, *J. Geophys. Res.*, *111*, E12S16, doi:10.1029/2006JE002762.
Johnson, J. R., W. M. Grundy, M. T. Lemmon, J. F. Bell, M. J. Johnson, R. G. Deen, R. E. Arvidson, W. H. Farrand, E. A. Guinness, and A. G. Hayes (2006b), Spectrophotometric properties of materials observed by Pancam on the Mars Exploration Rovers: 1. Spirit, *J. Geophys. Res.*, *111*, E02S14, doi:10.1029/2005JE002494.
Johnson, J. R., et al. (2017), Visible/near-infrared spectral diversity from in situ observations of the Bagnold Dune Field sands in Gale crater, Mars, *J. Geophys. Res. Planets*, *122*, doi:10.1002/2016JE005187.
Kocurek, G., and R. C. Ewing (2012), Source-to-sink: An Earth/Mars comparison of boundary conditions for eolian dune systems, in *Sedimentary Geology of Mars*, edited by J. P. Grotzinger and R. E. Milliken, *SEPM Spec. Publ.*, *102*, 151–168, doi:10.2110/pec.12.102.0151.
Kok, J. F. (2010a), Difference in the wind speeds required for initiation versus continuation of sand transport on Mars: Implications for dunes and dust storms, *Phys. Rev. Lett.*, *104*(7), 074502, doi:10.1103/PhysRevLett.104.074502.
Kok, J. F. (2010b), An improved parameterization of wind-blown sand flux on Mars that includes the effect of hysteresis, *Geophys. Res. Lett.*, *37*, L12202, doi:10.1029/2010GL043646.
Kok, J. F., E. J. Parteli, T. I. Michaels, and D. B. Karam (2012), The physics of wind-blown sand and dust, *Rep. Prog. Phys.*, *75*(10), 106901, doi:10.1088/0034-4885/75/10/106901.
Kreisch, C. D., J. A. O'Sullivan, R. E. Arvidson, D. V. Politte, L. He, N. T. Stein, J. Finkel, E. A. Guinness, M. J. Wolff, and M. G. A. Lapotre (2017), Regularization of Mars Reconnaissance Orbiter CRISM along-track oversampled hyperspectral imaging observations of Mars, *Icarus*, *182*, 136–151, doi:10.1016/j.icarus.2016.09.033.
Lane, M. D., and P. R. Christensen (2013), Determining olivine composition of basaltic dunes in Gale crater, Mars, from orbit: Awaiting ground truth from Curiosity, *Geophys. Res. Lett.*, *40*, 3517–3521, doi:10.1002/grl.50621.
Lapotre, M., et al. (2016), Large wind ripples on Mars: A record of atmospheric evolution, *Science*, *353*(6294), 55–58, doi:10.1126/science.aaf3206.
Lapotre, M. G. A., B. L. Ehlmann, and S. E. Minson (2017), A probabilistic approach to remote compositional analysis of planetary surfaces, *J. Geophys. Res. Planets*, *122*, 983–1009, doi:10.1002/2016JE005248.
Li, S., and R. E. Milliken (2015), Estimating the modal mineralogy of eucrite and diogenite meteorites using visible–near infrared reflectance spectroscopy, *Meteorit. Planet. Sci.*, *50*(11), 1821–1850, doi:10.1111/maps.12513.
Lucey, P. G. (1998), Model near-infrared optical constants of olivine and pyroxene as a function of iron content, *J. Geophys. Res.*, *103*(E1), 1703–1713.
Makse, H. A. (2000), Grain segregation mechanism in aeolian sand ripples, *Eur. Phys. J. E: Soft Matter Biol. Phys.*, *1*(2–3), 127–135, doi:10.1007/pl00014592.
Mangold, N., D. Baratoux, O. Arnalds, J.-M. Bardintzeff, B. Platevoet, M. Gregoire, and P. Pinet (2011), Segregation of olivine grains in volcanic sands in Iceland and implications for Mars, *Earth Planet. Sci. Lett.*, *310*(3), 233–243, doi:10.1016/j.epsl.2011.07.025.
Mason, C. C., and R. L. Folk (1958), Differentiation of beach, dune, and aeolian flat environments by size analysis, Mustang Island, Texas, *J. Sediment. Res.*, *28*(2), 211–226.
Milliken, R., J. Grotzinger, and B. Thomson (2010), Paleoclimate of Mars as captured by the stratigraphic record in Gale crater, *Geophys. Res. Lett.*, *37*, L04201, doi:10.1029/2009GL041870.
Milliken, R., R. C. Ewing, W. Fischer, and J. Hurowitz (2014), Wind-blown sandstones cemented by sulfate and clay minerals in Gale crater, Mars, *Geophys. Res. Lett.*, *41*, 1149–1154, doi:10.1002/2013GL059097.
Minson, S., M. Simons, and J. Beck (2013), Bayesian inversion for finite fault earthquake source models-I: Theory and algorithm, *Geophys. J. Int.*, *194*(3), 1701–1726, doi:10.1093/gji/ggt180.
Minson, S., M. Simons, J. Beck, F. Ortega, J. Jiang, S. Owen, A. Moore, A. Inbal, and A. Sladen (2014), Bayesian inversion for finite fault earthquake source models-II: The 2011 great Tohoku-oki, Japan earthquake, *Geophys. J. Int.*, *198*(2), 922–940, doi:10.1093/gji/ggu170.
Murchie, S. L., F. P. Seelos, C. D. Hash, D. C. Humm, E. Malaret, J. A. McGovern, T. H. Choo, K. D. Seelos, D. L. Buczkowski, and M. F. Morgan (2009), Compact Reconnaissance Imaging Spectrometer for Mars investigation and data set from the Mars Reconnaissance Orbiter's primary science phase, *J. Geophys. Res.*, *114*, E00D07, doi:10.1029/2009JE003344.
Mustard, J. F., and C. M. Pieters (1987), Quantitative abundance estimates from bidirectional reflectance measurements, *J. Geophys. Res.*, *92*(B4), E617–E626.
Nesbitt, H. W., and G. M. Young (1996), Petrogenesis of sediments in the absence of chemical weathering: Effects of abrasion and sorting on bulk composition and mineralogy, *Sedimentology*, *43*(2), 341–358.
Newman, C. E., et al. (2017), Winds measured by the Rover Environmental Monitoring Station (REMS) during the Mars Science Laboratory (MSL) rover's Bagnold Dunes campaign and comparison with numerical modeling using MarsWRF, *Icarus*, *291*, 203–231, doi:10.1016/j.icarus.2016.12.016.
O'Connell-Cooper, C. D., et al. (2017), APXS-derived chemistry of the Bagnold Dune sands: Comparison with Gale crater soils and the global Martian average, *J. Geophys. Res. Planets*, *122*, doi:10.1002/2017JE005268.
Pan, C., and A. D. Rogers (2017), Occurrence and scale of compositional heterogeneity in Martian dune fields: Toward understanding the effects of aeolian sorting on Martian sediment compositions, *Icarus*, *282*, 56–69, doi:10.1016/j.icarus.2016.09.021.
Parfenoff, A., C. Pomerol, and J. Tourenq (1970), *Les Mineraux en grains: methodes d'etude et determination*, p. 578, Masson et Cie, Paris.
Poulet, F., and S. Erard (2004), Nonlinear spectral mixing: Quantitative analysis of laboratory mineral mixtures, *J. Geophys. Res.*, *109*, E02009, doi:10.1029/2003JE002179.
Poulet, F., N. Mangold, B. Platevoet, J.-M. Bardintzeff, V. Sautter, J. Mustard, J.-P. Bibring, P. Pinet, Y. Langevin, and B. Gondet (2009), Quantitative compositional analysis of Martian mafic regions using the MEx/OMEGA reflectance data: 2. Petrological implications, *Icarus*, *201*(1), 84–101, doi:10.1016/j.icarus.2008.12.042.
Robertson, K. M., R. E. Milliken, and S. Li (2016), Estimating mineral abundances of clay and gypsum mixtures using radiative transfer models applied to visible-near infrared reflectance spectra, *Icarus*, *277*, 171–186, doi:10.1016/j.icarus.2016.04.034.

Rogers, A. D., and J. L. Bandfield (2009), Mineralogical characterization of Mars Science Laboratory candidate landing sites from THEMIS and TES data, *Icarus*, *203*(2), 437–453, doi:10.1016/j.icarus.2009.04.020.

Sautter, V., M. Toplis, R. Wiens, A. Cousin, C. Fabre, O. Gasnault, S. Maurice, O. Forni, J. Lasue, and A. Ollila (2015), In situ evidence for continental crust on early Mars, *Nat. Geosci.*, *8*(8), 605–609, doi:10.1038/ngeo2474.

Seelos, K. D., F. P. Seelos, C. E. Viviano-Beck, S. L. Murchie, R. E. Arvidson, B. L. Ehlmann, and A. A. Fraeman (2014), Mineralogy of the MSL Curiosity landing site in Gale crater as observed by MRO/CRISM, *Geophys. Res. Lett.*, *41*, 4880–4887, doi:10.1002/2014GL060310.

Shao, Y., and H. Lu (2000), A simple expression for wind erosion threshold friction velocity, *J. Geophys. Res.*, *105*(D17), 22,437–22,443, doi:10.1029/2000JD900304.

Siebach, K. L., S. M. McLennan, and C. M. Fedo (2017), Geochemistry of the Stimson Sandstone, Gale Crater, Mars, *Proc. Lunar Planet. Sci. Conf. 48th*, The Woodlands, Tex.

Silvestro, S., D. Vaz, R. Ewing, A. Rossi, L. Fenton, T. Michaels, J. Flahaut, and P. Geissler (2013), Pervasive aeolian activity along rover Curiosity's traverse in Gale crater, Mars, *Geology*, *41*(4), 483–486, doi:10.1130/G34162.1.

Silvestro, S., D. A. Vaz, H. Yizhaq, and F. Esposito (2016), Dune-like dynamic of Martian aeolian large ripples, *Geophys. Res. Lett.*, *43*, 8384–8389, doi:10.1002/2016GL070014.

Stamnes, K., S.-C. Tsay, W. Wiscombe, and K. Jayaweera (1988), Numerically stable algorithm for discrete-ordinate-method radiative transfer in multiple scattering and emitting layered media, *Appl. Opt.*, *27*(12), 2502–2509.

Stockstill-Cahill, K. R., F. S. Anderson, and V. E. Hamilton (2008), A study of low-albedo deposits within Amazonis Planitia craters: Evidence for locally derived ultramafic to mafic materials, *J. Geophys. Res.*, *113*, E07008, doi:10.1029/2007JE003036.

Sullivan, R., R. Arvidson, J. Bell, R. Gellert, M. Golombek, R. Greeley, K. Herkenhoff, J. Johnson, S. Thompson, and P. Whelley (2008), Wind-driven particle mobility on Mars: Insights from Mars Exploration Rover observations at El Dorado and surroundings at Gusev crater, *J. Geophys. Res.*, *113*, E06S07, doi:10.1029/2008JE003101.

Tirsch, D., R. Jaumann, A. Pacifici, and F. Poulet (2011), Dark aeolian sediments in Martian craters: Composition and sources, *J. Geophys. Res.*, *116*, E03002, doi:10.1029/2009JE003562.

Viviano-Beck, C. E., F. P. Seelos, S. L. Murchie, E. G. Kahn, K. D. Seelos, H. W. Taylor, K. Taylor, B. L. Ehlmann, S. M. Wisemann, and J. F. Mustard (2014), Revised CRISM spectral parameters and summary products based on the currently detected mineral diversity on Mars, *J. Geophys. Res. Planets*, *119*, 1403–1431, doi:10.1002/2014JE004627.

Zeidler, S., T. Posch, H. Mutschke, H. Richter, and O. Wehrhan (2011), Near-infrared absorption properties of oxygen-rich stardust analogs—The influence of coloring metal ions, *Astron. Astrophys.*, *526*, A68, doi:10.1051/0004-6361/201015219.